

SLAC - PUB - 4160

December 1986

T/E

**Measurements of total hadronic and inclusive  
 $D^*$  cross sections in  $e^+ e^-$  annihilations  
between 3.87 and 4.5 GeV\***

A. Osterheld<sup>(a)</sup>, R. Hofstadter, R. Horisberger,<sup>(b)</sup> I. Kirkbride, H. Kolanoski,<sup>(c)</sup>  
K. Königsmann,<sup>(d)</sup> A. Liberman,<sup>(e)</sup> J. O'Reilly,<sup>(f)</sup> and J. Tompkins<sup>(g)</sup>

*Physics Department and High Energy Physics Laboratory,  
Stanford University, Stanford, California 94305*

and

R. Partridge,<sup>(h)</sup> C. Peck, and F.C. Porter

*Physics Department, California Institute of Technology, Pasadena, California 91125*

and

Y.F. Gu,<sup>(i)</sup> W. Kollman,<sup>(j)</sup> K. Strauch, and K. Wacker<sup>(k)</sup>

*Lyman Laboratory of Physics, Harvard University, Cambridge, Massachusetts 02138*

and

D. Aschman,<sup>(l)</sup> T. Burnett,<sup>(m)</sup> M. Cavalli-Sforza,<sup>(n)</sup> R. Cowan,<sup>(o)</sup>

D. Coyne,<sup>(n)</sup> and H.F.W. Sadrozinski<sup>(n)</sup>

*Physics Department, Princeton University, Princeton, New Jersey 08544*

and

E. Bloom, F. Bulos, R. Chestnut,<sup>(p)</sup> J. Gaiser,<sup>(q)</sup> G. Godfrey, C. Kiesling,<sup>(r)</sup>

W. Lockman,<sup>(n)</sup> and M. Oreglia<sup>(s)</sup>

*Stanford Linear Accelerator Center, Stanford University, Stanford, California 94305*

*(Submitted to Physical Review D)*

---

\* Work supported in part by the Department of Energy under contracts DE-AC03-76SF00515 (SLAC), DE-AC02-76ER03064 (Harvard), DE-AC03-81ER40050 (CIT), and DE-AC02-76ER03072 (Princeton); by the National Science Foundation contracts PHY81-07396 (HEPL), PHY79-16461 (Princeton), and PHY75-22980 (CIT); by the NATO Fellowship (HK), the Chaim Weizmann Fellowship (FP), and the Sloan Foundation (TB).

## ABSTRACT

Total hadronic and inclusive  $D^*$  cross sections have been measured by the Crystal Ball detector at SPEAR in  $e^+e^-$  annihilation at center of mass energies in the resonance region (3.87–4.5 GeV) above open charm threshold. The prominent features of the hadronic cross section are a resonance at 4.03 GeV, a broad shoulder near 4.16 GeV, a valley around 4.2 GeV, and a broader peak at 4.4 GeV. An additional data point at 3.67 GeV allows a comparison to energies below open charm threshold. The production of  $D^*$  mesons is deduced from a low energy peak in the  $\pi^0$  kinetic energy spectrum (below 50 MeV) arising from  $D^{*(0,+)} \rightarrow \pi^0 D^{(0,+)}$ . The shape of this cross section is qualitatively similar to the total hadronic cross section. The two results are combined to yield the average number of  $D^*$  mesons per charm event. This number is approximately 1 between  $D^*\bar{D}$  and  $D^*\bar{D}^*$  threshold and 1.5–2 at higher energies.

## I. INTRODUCTION

The study of hadron production in the charm resonance region of  $e^+e^-$  annihilation (3.0–5.0 GeV) has played an important role in advancing our understanding of subatomic particles and their interactions. The size of  $R$ , the ratio of hadronic to  $\mu$ -pair cross sections, was an important underpinning of the quark-parton model. An investigation of the energy behavior of  $R$  led to the observation of a new quark flavor. This flavor, charm, had earlier been proposed for symmetry reasons and to explain the absence of strangeness changing weak neutral currents.<sup>1,2</sup> Studies of charmed hadron final states have further elucidated the phenomenology of particle physics.

The charmonium model<sup>3</sup> of Appelquist and Politzer describes  $c\bar{c}$  mesons as a quark-antiquark pair bound in a central potential. Because of the large mass of the charmed quark, a non-relativistic description may be employed. The vector  $1^3S_1$  and  $2^3S_1$  states may be produced directly in  $e^+e^-$  annihilation and are observed as the narrow  $J/\psi(3095)$ <sup>4</sup> and  $\psi'(3684)$ <sup>5</sup> resonances. A broader state,  $\psi''(3772)$ <sup>6</sup>, lies slightly above open charm threshold and decays predominantly into  $D\bar{D}$  states.

Between 3.8 and 4.5 GeV,  $R$  displays a complicated structure associated with the production of pairs of open charm hadrons, which contain a charmed and a light quark.

Phenomenological models have been developed to explain the behavior of the open charm cross section. The coupled channel model<sup>7</sup> of Eichten *et al.* is an extension of a charmonium model which assumes a potential of the form

$$V(r) = -\frac{\kappa}{r} + \frac{r}{a^2} \quad [I.1]$$

where  $r$  is the quark anti-quark separation. The model is extended by allowing the potential to operate between quarks of different flavors, with the assumption that the potential is flavor independent. It is also assumed that charm production is mediated by  $c\bar{c}$  states coupling directly to the annihilation photon, and the entire problem is treated non-relativistically. The charmonium state decays after the creation of light quark pairs by the potential, and the charm cross section is described as a sum of quasi two-body charmed meson cross sections.

The behavior of the charm cross section in  $e^+e^-$  annihilation in the region  $3.87 \leq E_{cm} \leq 4.5$  GeV is the subject of this investigation.<sup>8</sup> The first topic in this report is a measurement of the total hadronic cross section using the calorimetric properties of the Crystal Ball detector. This high statistics measurement illuminates the structure of  $\sigma_{had}$  at these energies. The second investigation probes the source of the structure in the total cross section by measuring the cross section for the process  $e^+e^- \rightarrow D^* + X$ . These results are compared to previous measurements, and to the predictions of the coupled channel model.

## II. CRYSTAL BALL DETECTOR

The main features of the Crystal Ball detector are summarized here. More detailed descriptions may be obtained elsewhere.<sup>9</sup> The detector components important for this analysis are a central array of NaI(Tl) scintillator crystals,

an inner charged particle tracking system, and a small angle luminosity monitor. Supplementary endcap crystal arrays were not used in this analysis.

The heart of the Crystal Ball detector (see fig. 1) is the central array of 672 NaI(Tl) crystals, covering 93% of the total solid angle. Photons and electrons induce electromagnetic showers in the crystals and deposit virtually all of their energy. Minimum ionizing particles deposit a characteristic energy of roughly 210 MeV, and interacting hadronic particles deposit an intermediate amount of energy in a typically irregular pattern. Under experimental conditions, the central ball achieves a photon energy resolution  $\sigma_E/E \approx 0.028/E^{1/4}$  ( $E$  in GeV) and an energy dependent photon angular resolution of 1–2 degrees.

The inner tracking system was used to tag tracks charged particle candidates, and to determine their directions if a sufficient number of aligned chamber hits were observed. The tracking system consisted of two sets of cylindrical spark chambers, separated by a multi-wire proportional chamber (MWPC).<sup>10</sup> The innermost spark chamber covered 93% of  $4\pi$  solid angle.

The luminosity was monitored by a precision, small angle luminosity detector, which measured Bhabha scattering counting rates. The monitor consisted of four telescope arms located symmetrically about the interaction point. A comparison with large angle  $e^+e^-(\gamma)$  and  $\gamma\gamma(\gamma)$  rates<sup>11</sup> indicated that the precision of the luminosity measured in this manner is  $\pm 4\%$ .

The triggering system used fast analog energy sums of groups of nine crystals and information from the MWPC's. Triggers were only accepted within  $\pm 40$  nsec of the beam timing signal, which reduced the cosmic ray background.

A trigger was generated if at least one of the following conditions was satisfied.

1. The total energy of the central ball exceeded 1150 MeV.
2. There was a pair of opposing minor triangles<sup>12</sup> each containing at least 60 MeV.
3. At least two major triangles<sup>12</sup> had energies greater than 140 MeV and hits were found in two MWPC planes.

4. Both the top and bottom hemispheres had at least 144 MeV and the total energy was greater than 770 MeV.

Studies have shown<sup>11</sup> that these triggers were at least 99% efficient for hadronic events satisfying the hadron selection requirements described below.

### III. TOTAL HADRONIC CROSS SECTIONS

The Crystal Ball detector is particularly well-suited to a total cross section measurement. The central portion of the detector covers a large portion (93%) of the solid angle in a homogeneous manner. The high degree of segmentation allows the classification of events according to the spatial distribution of energy. The detector measures the total energy of neutral particles and detects some portion of the charged energy. These excellent calorimetric properties reduce the  $E_{cm}$  variation of the hadronic acceptance, and the model dependence of the Monte Carlo simulation.

#### A. Method of Determining $R$

The total hadronic cross section is normally presented as a ratio,  $R$ , defined as

$$R = \frac{\sigma_{had}^0}{\sigma_{\mu\mu}^0} = \frac{N_{had}^0}{L\sigma_{\mu\mu}^0}. \quad [III.1]$$

Here  $L$  is the integrated luminosity of the data, and  $N_{had}^0$  is the number of one-photon annihilation hadronic events produced, a number to be estimated from the data. The lowest order QED muon pair cross section is calculated from

$$\sigma_{\mu\mu}^0 = \frac{4\pi\alpha^2}{3s} = \frac{86.8}{E_{cm}^2} \text{ nb}, \quad [III.2]$$

where  $E_{cm}$  is measured in GeV.

The detector is triggered by hadronic events, cosmic ray events, beam-gas and beam-wall collisions, two-photon annihilation events ( $e^+e^- \rightarrow e^+e^- + X$ ), and

the QED processes  $e^+e^-(\gamma)$ ,  $\gamma\gamma(\gamma)$ ,  $\mu^+\mu^-(\gamma)$ , and  $\tau^+\tau^-(\gamma)$ . The hadron selection algorithm classifies events according to their patterns of energy deposition and counts the number of hadronic candidates,  $N_{sel}$ , and the number of beam gas candidates,  $N_{bgcut}$ . Residual backgrounds contaminating  $N_{sel}$  are statistically subtracted. The beam gas subtraction assumes that the beam gas contribution to  $N_{sel}$  scales in proportion to the beam gas contribution to  $N_{bgcut}$ . The proportionality constant,  $h_{bg}$ , is obtained from separated beam data. The number of hadronic events is given by

$$N_{had} = \frac{N_{sel} - h_{bg}N_{bgcut} - \sum_i (h_i - h_{bg}b_i)n_i}{\bar{\epsilon}^{eff}} \quad [III.3]$$

where

$$\bar{\epsilon}^{eff} = \bar{\epsilon} - h_{bg}\bar{b}_{had}. \quad [III.4]$$

Here  $\bar{\epsilon}$  is the average hadronic efficiency,  $n_i$  is the number of events of type  $i$ , and  $h_i$  and  $b_i$  are the fractions of those events that contribute to  $N_{sel}$  and  $N_{bgcut}$ . The sum runs over all background types other than beam gas events. The bar on  $\bar{\epsilon}^{eff}$  and  $\bar{b}_{had}$  emphasizes that these quantities are averaged over all hadronic events, including radiative events.

The first two terms in the numerator on the right side of eqn. [III.3] would yield the visible number of hadrons if  $N_{sel}$  contained only hadronic and residual beam-gas events, and  $N_{bgcut}$  contained only beam-gas events. The rest of the numerator corrects for the events of other types that spill into  $N_{sel}$  and  $N_{bgcut}$ . The difference between the effective efficiency  $\bar{\epsilon}^{eff}$  and the efficiency  $\bar{\epsilon}$  accounts for the number of hadronic events that leak into  $N_{bgcut}$ , causing one to over-subtract in the beam-gas correction.

The quantity  $R$  represents only the contribution from the single-photon annihilation term. The process of estimating and removing the higher order contributions, called radiative corrections, is discussed in detail in Appendix A. This correction is represented by a factor  $1 + \delta$ . It is useful to move the

radiative effects in  $\bar{\epsilon}^{eff}$  into the radiative correction factor, making the replacement  $\bar{\epsilon}^{eff}(1 + \delta) = \epsilon^{eff}(0)(1 + \delta_{obs})$ . Here  $\epsilon^{eff}(k)$  is the effective efficiency for events with a radiative photon of energy  $k$ , and  $\delta_{obs}$  contains a modification of the bremsstrahlung term to reflect the  $k$ -dependence of the hadronic acceptance. It is also useful to separate the effect of radiation to the narrow resonances from the bremsstrahlung term. Then

$$R = \frac{N_{sel} - h_{bg}N_{bgcut} - \sum_i (h_i - h_{bg}b_i) n_i - \sum_j L\epsilon_{tail,j}^{eff} \sigma_{tail}^j}{L\sigma_{\mu\mu}^0 \epsilon^{eff}(0)(1 + \delta_{obs})}. \quad [III.5]$$

Application of this formula requires an event selection algorithm to estimate  $N_{sel}$  and  $N_{bgcut}$ , the determination of  $h_{bg}$  from separated beam data, and the estimation of  $\epsilon^{eff}$ ,  $h_i$ ,  $b_i$  from Monte Carlo simulations.

## B. Event Selection

The primary hadron selection was based on criteria developed for a Crystal Ball study of hadron production in the 5–7 GeV region.<sup>11</sup> In analyzing the data for these measurements, modifications to the criteria of reference 11 were necessary. Specifically, the determination and suppression of beam-gas background require a more stringent cut which (on average) reduced the beam-gas contamination by a factor of three.

In the Crystal Ball detector, ‘tracks’ are defined as contiguous regions of energy deposition; track direction is determined from the energy deposition around the crystal with the maximum energy in the region. Tracks are labeled charged if their directions are correlated with signals in the central tracking detector. In the selection criteria outlined below, both the individual crystal energies and the reconstructed tracks are used to determine event characteristics. The event topology—the global energy deposition pattern as measured in the NaI(Tl)—is an important component of the selection process.

Hadron candidates were required to satisfy the following conditions:

1. *QED cut*: events were rejected as being  $e^+e^-(\gamma)$ , or  $\gamma\gamma(\gamma)$  if more than one track had more than half the beam energy, or if any track had more than 75% of the beam energy and there were fewer than four regions with at least 50 MeV of energy.
2. *multiplicity cut*: at least 3 regions with at least 50 MeV of energy. In addition, an event with no charged tracks was required to have at least 35% of the center of mass energy.
3. *beam-gas cut*: The beam-gas requirement removed events with low transverse momentum relative to the beam axis; the requirement was more stringent for events with large energy asymmetries, or small fractions of  $E_{cm}$  visible in the detector. The number of events that failed this cut comprised the beam gas sample and was used as a measure of the beam conditions to normalize the beam-gas subtraction.
4. *jettiness cut*: An "energy-momentum" tensor was defined as

$$P_{ij} = \sum_k E_k^2 (\delta_{ij} - n_i^k n_j^k) \quad [III.6]$$

where  $E_k$  and  $n_i^k$  are the energy and direction cosines of the  $k$ th crystal, respectively. The smallest eigenvalue of  $P_{ij}$ ,  $p_{t-jet}^2$ , is a measure of the momentum-squared transverse to the jet axis; events with collimated energy distributions have low  $p_{t-jet}^2$ . Events were required to satisfy

$$A \equiv \frac{|\sum_k E_k \hat{n}_k|}{\sum_k E_k} \leq [\log_{10}(p_{t-jet}^2) + 2.8] / 1.8. \quad [III.7]$$

The requirement on  $p_{t-jet}^2$  was larger for events with larger energy-weighted asymmetries,  $A$ . This cut was designed to remove any cosmic rays and  $\mu^+\mu^-(\gamma)$  events that remained in the sample.

5. *front-back asymmetry cut*: Events were required to have

$$\frac{|\sum_{z>0} E_i - \sum_{z<0} E_i|}{\sum_i E_i} \leq 0.8 \quad [III.8]$$



where  $z$  refers to the beam direction.

Requirements 1–5 comprise the preliminary selection. Many of the separated beam events that passed these cuts were quite asymmetric, though not necessarily in the forward-backward direction. An approximate algorithm was developed to find a plane (defined by the unit vector  $\hat{n}_{max}$ ) that divided the ball into two hemispheres whose energies were as different as possible.

6. *maximum asymmetry cut*: The maximum asymmetry was defined by

$$A_{max} = \max \frac{|\sum_i E_i \theta(\hat{n}_i \cdot \hat{n}_{max}) - \sum_i E_i \theta(-\hat{n}_i \cdot \hat{n}_{max})|}{\sum_i E_i} \quad [III.9]$$

where  $\theta(x)$  is the Heaviside step function. The maximization algorithm restricted  $\hat{n}_{max}$  to the 720 (real and missing) crystal direction vectors. Events were required to satisfy:

$$A_{max} \leq 0.85 \quad [III.10]$$

Figure 2 displays beam timing and visible energy fraction distributions for the original and hadron selected data samples from a typical data tape. The original data sample predominantly consists of high energy  $e^+e^-(\gamma)$  and  $\gamma\gamma(\gamma)$  events, and low energy cosmic ray (uncorrelated with the beam collision time) and beam-gas events.

### C. Event Simulation and Backgrounds

On a typical data tape, roughly equal numbers of showering QED, cosmic ray, and beam-gas events account for approximately 96% of the events. The remaining 4% consists of  $\mu^+\mu^-(\gamma)$ ,  $\tau^+\tau^-(\gamma)$ , two photon, and hadronic events. The beam-gas and cosmic ray backgrounds were studied using separated-beam data, and the hadronic events and the remaining backgrounds were investigated using Monte Carlo techniques.

The Crystal Ball Monte Carlo simulation is comprised of two sections: an event generator which creates final state configurations with parameters distributed

according to appropriate physical models and decays unstable particles according to known or suspected decay modes, and a detector simulation section which propagates the particles through the detector, depositing energy by a simulation of the microscopic interactions of the particles with the detector components. The simulation of electromagnetically interacting particles was handled by the Electron Gamma Shower (EGS) code,<sup>13</sup> while hadronic interactions were simulated by the High Energy Transport Code<sup>14</sup> (HETC). In addition, the detector simulation generated sparks and noise hits in the inner tracking chambers.

Three types of hadron models were used. One model simulated light ( $u, d, s$ ) quark physics by generating a collection of  $\pi$ ,  $K$ , and  $\eta$  mesons according to a phase space model. The generated particle multiplicities were Poisson distributed about mean values adjusted to bring the observed multiplicity distribution into agreement with the data. Charm production was modeled by generating pairs of charmed  $D$  and  $D^*$  mesons. The cascade decays of the  $D^*$  mesons were generated according to measured branching ratios,<sup>15</sup> and the ground state  $D$  mesons were decayed according to the constant matrix element model of Quigg and Rosner<sup>16</sup>. Some additional leptonic decays were added to bring the multiplicity distributions into agreement with the observed  $D^+$  and  $D^0$  distributions.<sup>17</sup> The final hadronic model employed was the 1981 version of the Lund fragmentation model<sup>18</sup> which was used to model both light quark and charm events. This model generated quark jets, which were then hadronized into observable particles.

The same algorithm was used to generate radiative events in all three models. The algorithm generated a spectrum of radiative photons as if  $R$  were constant. The energy available to the hadron model was reduced, the hadronic system was generated and then Lorentz boosted opposite the radiative photon. Since  $R$  is not constant, this simulation does not directly yield the hadron acceptance. Instead, this method was used to determine the acceptance as a function of the energy of the radiative photon. This acceptance function was then folded into the bremsstrahlung spectrum generated using a non-constant  $R$  as described in

appendix A. The efficiencies quoted here have been extrapolated to the case of zero-energy radiative photons.

The average charm efficiency was determined to be  $0.93 \pm 0.03$ . The acceptance for light quark events was interpolated between 0.84 and 0.87 at 3.67 and 4.47 GeV, respectively. The light quark and charm acceptances were weighted using the  $E_{cm}=3.67$  GeV point to estimate light quark production. The fraction misidentified as beam-gas, averaged over all of the hadron Monte Carlos is  $b_{had}=0.021$ .

There are four distinct types of QED events to be considered:  $e^+e^-(\gamma)$ ,  $\gamma\gamma(\gamma)$ ,  $\mu^+\mu^-(\gamma)$ , and  $\tau^+\tau^-(\gamma)$ . All were modeled after Berends-Kleiss event generators<sup>19</sup> which include contributions to  $O(\alpha^3)$ . Only the  $\tau^+\tau^-(\gamma)$  events constituted a significant background. Since  $\tau$  leptons decay into hadrons a substantial portion of the time, these events mimic typical hadronic events. However, they tend to be jettier, more asymmetric and have lower multiplicity. Typically 31–36% of the  $\tau$  events are identified as hadrons, and 10–12% are identified as beam-gas events. The  $\tau^+\tau^-(\gamma)$  events account for about 5–7% of the hadron sample. The remaining QED event types account for less than 1% of the hadron sample and much less than 1% of the beam-gas sample and are not considered further.

Events arising from two photon processes are a very small background at these energies: the  $\gamma\gamma$  energy is small and the  $\gamma\gamma$  system is typically moving with respect to the detector, which reduces acceptance. The two photon events were modeled using an Equivalent Photon Approximation<sup>20</sup> and were found to contribute roughly 1% of the final hadronic sample. Uncertainties in the determination of  $b_{2\gamma}$  contribute a 0.5% uncertainty in  $R$ .

Residual cosmic ray backgrounds can be determined from timing distributions. Events unrelated to the beam crossing account for less than 1% of the hadronic sample, and 2–3% of the beam-gas candidates.

Beam gas events constitute the most serious background in this analysis.

Separated beam data (taken with both beams circulating in the ring, but not colliding) were used to determine  $h_{bg}$ , the constant used to estimate the number of beam-gas events called hadrons from those labeled ‘beam-gas’. This constant was observed to be independent of  $E_{beam}$ , and the separated beam data were averaged to obtain  $h_{bg} = 0.028 \pm 0.003$ . Typically 3% of the hadronic sample are beam-gas events. Under poor beam conditions, this may increase by a factor of two or three. A comparison of  $R$ -values (at the same energy) from data collected at widely separated times indicated that this value of  $h_{bg}$  correctly accounts for the beam-gas contamination under differing beam conditions.<sup>8</sup>

#### D. Radiative Corrections

The radiative correction procedure is described in detail in appendix A. This procedure extracts the one-photon annihilation cross section by estimating and removing contributions from processes with additional photon couplings. This lowest order cross section displays the fundamental behavior of the photon-hadron coupling. In contrast, some higher order terms reflect the behavior at all energies and include purely electromagnetic effects. Even if they are not removed from the cross section, these higher order contributions must be understood, since they alter the acceptance calculation.

Rewriting eq. [III.5],

$$R = \frac{R^{norad} - \sum_j \frac{\epsilon_{tail,j}^{eff}}{\epsilon_{eff}(0)} R_{tail,j}}{1 + \delta_{obs}} \quad [III.11]$$

where  $R^{norad}$  is  $R$  calculated as if no radiative effects were present, and the bremsstrahlung integral included in  $\delta_{obs}$  has been modified to reflect the acceptance for radiative events. (Note that  $R^{norad}$  is a detector dependent quantity.)

The radiative corrections were approximated by the first order QED corrections to the initial state. These include contributions from the initial state

vertex correction, modifications of the annihilation photon propagator by inserting  $e^+e^-$ ,  $\mu^+\mu^-$ ,  $\tau^+\tau^-$ , and quark-antiquark pair vacuum polarization loops, and bremsstrahlung radiation from the initial state charged particles. These corrections depend upon detector acceptances and upon the  $E_{cm}$  dependence of  $R$ .

The final state correction is small because of the KNL cancellations<sup>22</sup> from summing over degenerate states. (These cancellations do not occur in the initial state radiative correction, since the storage ring selects a particular  $e^+e^-$  state.) The magnitude of the final state correction is model dependent, but is roughly 0.5% and is neglected in this measurement. Higher order radiative corrections have been estimated using a renormalization group calculation.<sup>23</sup> It is estimated that the higher order terms neglected by the first order radiative correction are bounded by 1%.

The radiative corrections depend on the shape of  $R$  itself, and the correction was calculated using an iterative technique. The  $R$  values measured by this experiment were smoothed before they were used in the radiative correction calculation, to avoid amplifying statistical fluctuations. Figure 3 demonstrates the radiative correction procedure. The curve is a smoothed representation of  $R$  values calculated as if no radiative effects were present. The data points are the  $R$  values corrected using the curve as input to the radiative correction algorithm. These corrected points were then smoothed, the radiative terms were recalculated, and the data points corrected according to these new values, etc. The additional corrections from further iterations are small. Because of the radiative effects in the acceptance, it is more meaningful to quote the product of the efficiency and radiative corrections. This total correction, including the tails of the narrow resonances, varies between 0.89 and 1.05. As may be seen, the main effects of the radiative corrections are to enhance the structure at 4.03 GeV and the valley around 4.2 GeV.

The function used to smooth the  $R$  values function has sufficient flexibility to accommodate the significant structures in the cross section, but may underestimate

the small scale structure in some regions. (Since this energy region is above open charm threshold, no narrow structures are expected.) For comparison, the radiative corrections were also calculated using a linear interpolation of the unsmoothed  $R$  values. Because of the sizeable statistical errors, this procedure overestimates the structure in the cross section. Except for a few single bin deviations, the results using the unsmoothed  $R$  values fluctuated by roughly 1–2% around the results obtained using the smoothed representation of  $R$ .

### E. Results for $R$

Figure 4 and table I present the results of this  $R$  measurement. The errors on the data points are the statistical errors from the number of counted hadrons and beam-gas events, as well as the point to point systematic error arising from the 20% uncertainty in the parameter  $h_{bg}$  (typically 0.5% of the  $R$  value). There are additional sources of systematic error. These include a normalization error of 4% from the luminosity and a normalization error of 10% of the hadron inefficiency which yields an error in  $R$  of 2%. There is an additional 2% point to point error from center of mass energy variations in the hadron production mechanism. Estimating the uncertainties in  $h_{tau}$  and  $h_{2\gamma}$  to be 10% yields uncertainties in  $R$  of 0.02–0.03 and 0.006 units of  $R$  respectively. Cutoffs in the  $2\gamma$  Monte Carlo give an additional 0.01 units of  $R$  systematic error from the correction to the beam-gas subtraction. The 2% error in the radiative correction arises from roughly equal contributions due to modeling the hadronic acceptance of hard radiative events, cutoffs required to calculate the bremsstrahlung integral, and from an assumed 20% uncertainty in  $R$  below 3.0 GeV. In the immediate vicinity of the 4.03 GeV resonance, this systematic grows to 4%. Overall, the normalization error is estimated to be 7%, with an additional point to point systematic error of 5%.

A comparison of this result to previously published measurements<sup>24–26</sup> of  $R$  in the resonance region is displayed in fig. 5. The  $R$  values measured in this

| $E_{cm}$ | $R$             | $E_{cm}$ | $R$             | $E_{cm}$ | $R$             | $E_{cm}$ | $R$             |
|----------|-----------------|----------|-----------------|----------|-----------------|----------|-----------------|
| 3.670    | $2.50 \pm 0.07$ | 4.022    | $4.72 \pm 0.24$ | 4.153    | $4.28 \pm 0.07$ | 4.292    | $2.98 \pm 0.08$ |
| 3.878    | $2.49 \pm 0.18$ | 4.028    | $4.68 \pm 0.10$ | 4.159    | $4.11 \pm 0.08$ | 4.304    | $3.34 \pm 0.09$ |
| 3.884    | $2.65 \pm 0.18$ | 4.034    | $4.82 \pm 0.17$ | 4.165    | $4.00 \pm 0.08$ | 4.316    | $3.23 \pm 0.09$ |
| 3.890    | $2.55 \pm 0.17$ | 4.040    | $4.54 \pm 0.14$ | 4.171    | $4.14 \pm 0.08$ | 4.328    | $3.32 \pm 0.09$ |
| 3.896    | $2.58 \pm 0.19$ | 4.046    | $4.61 \pm 0.11$ | 4.177    | $4.06 \pm 0.08$ | 4.340    | $3.43 \pm 0.09$ |
| 3.902    | $2.78 \pm 0.18$ | 4.052    | $4.43 \pm 0.09$ | 4.182    | $4.38 \pm 0.15$ | 4.352    | $3.44 \pm 0.06$ |
| 3.908    | $2.61 \pm 0.19$ | 4.058    | $4.29 \pm 0.09$ | 4.185    | $4.14 \pm 0.09$ | 4.364    | $3.65 \pm 0.09$ |
| 3.914    | $3.23 \pm 0.22$ | 4.064    | $4.01 \pm 0.09$ | 4.190    | $3.87 \pm 0.10$ | 4.376    | $3.75 \pm 0.09$ |
| 3.920    | $2.92 \pm 0.19$ | 4.070    | $4.04 \pm 0.11$ | 4.195    | $3.91 \pm 0.08$ | 4.382    | $3.86 \pm 0.16$ |
| 3.926    | $2.71 \pm 0.18$ | 4.076    | $4.06 \pm 0.11$ | 4.201    | $3.73 \pm 0.09$ | 4.388    | $3.82 \pm 0.09$ |
| 3.932    | $3.07 \pm 0.20$ | 4.082    | $3.92 \pm 0.11$ | 4.208    | $3.71 \pm 0.05$ | 4.394    | $3.99 \pm 0.21$ |
| 3.938    | $2.63 \pm 0.18$ | 4.088    | $4.07 \pm 0.11$ | 4.212    | $3.69 \pm 0.14$ | 4.400    | $4.00 \pm 0.08$ |
| 3.944    | $3.35 \pm 0.20$ | 4.094    | $4.03 \pm 0.11$ | 4.214    | $3.55 \pm 0.10$ | 4.406    | $3.79 \pm 0.21$ |
| 3.950    | $3.11 \pm 0.16$ | 4.100    | $4.14 \pm 0.11$ | 4.220    | $3.31 \pm 0.08$ | 4.412    | $3.94 \pm 0.08$ |
| 3.956    | $2.80 \pm 0.16$ | 4.105    | $4.03 \pm 0.09$ | 4.226    | $2.95 \pm 0.13$ | 4.418    | $4.03 \pm 0.11$ |
| 3.962    | $2.97 \pm 0.15$ | 4.109    | $4.06 \pm 0.15$ | 4.232    | $3.02 \pm 0.08$ | 4.424    | $4.02 \pm 0.06$ |
| 3.968    | $3.15 \pm 0.21$ | 4.113    | $4.19 \pm 0.08$ | 4.238    | $3.06 \pm 0.13$ | 4.430    | $4.09 \pm 0.11$ |
| 3.974    | $3.40 \pm 0.21$ | 4.118    | $4.06 \pm 0.08$ | 4.244    | $3.02 \pm 0.08$ | 4.436    | $4.05 \pm 0.09$ |
| 3.980    | $3.45 \pm 0.21$ | 4.121    | $4.20 \pm 0.06$ | 4.250    | $3.11 \pm 0.09$ | 4.442    | $3.89 \pm 0.20$ |
| 3.986    | $3.75 \pm 0.20$ | 4.125    | $4.21 \pm 0.07$ | 4.256    | $3.02 \pm 0.06$ | 4.448    | $3.92 \pm 0.10$ |
| 3.992    | $3.43 \pm 0.18$ | 4.129    | $4.14 \pm 0.08$ | 4.262    | $3.09 \pm 0.14$ | 4.460    | $3.85 \pm 0.20$ |
| 3.998    | $3.42 \pm 0.19$ | 4.133    | $4.08 \pm 0.11$ | 4.268    | $2.91 \pm 0.08$ | 4.472    | $3.84 \pm 0.20$ |
| 4.004    | $3.38 \pm 0.21$ | 4.136    | $4.02 \pm 0.11$ | 4.274    | $2.92 \pm 0.13$ | 4.484    | $3.61 \pm 0.21$ |
| 4.010    | $3.95 \pm 0.22$ | 4.141    | $4.09 \pm 0.08$ | 4.280    | $3.07 \pm 0.08$ | 4.496    | $3.72 \pm 0.21$ |
| 4.016    | $3.84 \pm 0.22$ | 4.147    | $4.24 \pm 0.08$ |          |                 |          |                 |

Table I. The  $R$  values plotted in fig. 4. The energies are in GeV.

analysis tend to be somewhat smaller than previously measured, particularly near the 4.4 GeV structure. In addition, there is some disagreement over the structure in the 4.06–4.2 GeV region. The DASP experiment assumed for their radiative corrections that the cross section in this region could be represented by the sum of two Breit-Wigner resonances. This would tend to enhance the separation between the two peaks. The Crystal Ball data were not consistent with the charmed portion of the cross section being a fermion threshold shape added incoherently to a sum of two or three Breit-Wigner resonances.

#### IV. INCLUSIVE $D^*$ CROSS SECTIONS

An important question in the resonance region above open charm threshold is the relative importance of different charm production mechanisms. While the total hadronic cross section in this energy region has been measured by several experiments, much less is directly known about individual charmed meson cross sections. This section describes a measurement of the inclusive cross section for the process  $e^+e^- \rightarrow D^* + X$ . For this measurement, the data between 3.87 and 4.5 GeV were divided into fourteen subsets. These  $E_{cm}$  steps were designed to isolate regions showing different structure in  $R$ .

##### A. Measuring $D^*$ Production using Low Energy $\pi^0$ Mesons

The technique we have used with the Crystal Ball takes advantage of the fact that the  $D^{*(0,+)} \rightarrow \pi^0 D^{(0,+)}$  cascade decays yield reasonably monochromatic (0–50 MeV)  $\pi^0$  mesons (“slow  $\pi^0$  mesons”), even well above threshold (see fig. 6). A measurement of the excess number of low energy  $\pi^0$  mesons yields an indirect measurement of the number of produced  $D^*$  mesons. Because of the large  $\pi^0$  cascade branching ratios of both  $D^{*0}$  and  $D^{*+}$  and the relatively large efficiency for reconstructing  $\pi^0$  mesons, this technique allows a detailed probe of the variation of the  $D^*$  cross section with center of mass energy.

The Crystal Ball is well suited to detecting  $\pi^0$  mesons through the  $\pi^0 \rightarrow \gamma\gamma$



(98.8%) decay. Its excellent photon angular and energy resolution and the large, uniform solid angle coverage provide the ability to reconstruct  $\pi^0$  mesons with high efficiency.

The distribution of  $\pi^0$  kinetic energies,  $T_{\pi^0}$ , is obtained from a two dimensional histogram of the kinetic energy  $T_{\gamma\gamma}$  versus the invariant mass  $m_{\gamma\gamma}$  of combinations of all pairs of photon candidates in an event. The invariant mass is calculated from  $m_{\gamma\gamma} = \sqrt{2E_1E_2(1 - \cos\theta_{12})}$ , where  $E_1$  and  $E_2$  are the energies<sup>27</sup> of the photon candidates and  $\theta_{12}$  is the angle between them. The kinetic energy is given by  $T_{\gamma\gamma} = E_1 + E_2 - m_{\gamma\gamma}$ . The two dimensional histogram in fig. 7 contains all of the data with  $3.87 \leq E_{cm} \leq 4.5$  GeV. The presence of  $\pi^0$  mesons is indicated by the ridge along the line  $m_{\gamma\gamma} \approx 135$  MeV. The projection of this  $\pi^0$  signal onto the  $T_{\gamma\gamma}$  axis yields the visible  $T_{\pi^0}$  spectrum. An excess of combinations in the region expected for  $D^*$  cascade  $\pi^0$  mesons (0–50 MeV) is clearly visible. The fitting procedure used to extract the excess number of  $\pi^0$  mesons in the  $D^*$  cascade region is described below.

## B. Photon Definition

The hadron selection used in this analysis is the preliminary selection described in Sec. III above. Since the data were gathered in a scan mode, the philosophy governing this analysis was to use fairly loose cuts which increase the  $\pi^0$  acceptance, but still yield smooth backgrounds in the  $T_{\gamma\gamma}$ - $m_{\gamma\gamma}$  histograms. The most important consideration is the shape of the background, especially the manner in which the shape changes as a function of  $T_{\gamma\gamma}$ . Because of energy-mass correlations, non-smooth background structures tend to propagate through the  $T_{\gamma\gamma}$ - $m_{\gamma\gamma}$  histogram in a manner that distorts the fitted  $T_{\pi^0}$  spectrum. The most serious background structure arises from combinations of minimum ionizing charged particles (characteristically 210 MeV) which eluded the charged particle tracking system and shower fluctuations identified as separate neutral tracks. These combinations interfere with the measurement of  $T_{\pi^0}$  in the region near

100 MeV.

The cuts used in the analysis to define “photons” are listed here.

1. *Solid angle cut*: The angle between the track direction and the beam axis,  $\theta_z$ , is required to satisfy  $|\cos \theta_z| \leq 0.9$ . This reduces the degradation of the energy resolution by eliminating tracks lying close to the tunnel region.
2. *Charge track cut*: Tracks which are associated with tracks in the charged particle detector are rejected. Approximately 2% of the  $\pi^0$  mesons are lost when one of the photons converts in the beam-pipe or inner detector and is tracked by the charged particle system.
3. *Shower fluctuation cut*: Fluctuations in the energy depositions of real particles may be identified as separate tracks. These spurious tracks are generally low in energy and found near other tracks. The energy associated with the track,  $E_{track}$ , and the angle to the nearest neighboring track are required to satisfy  $E_{track} > 240 (\cos \theta_{track-neigh} - 0.75)$ . In order to survive this cut, a track must have a higher energy when it is found nearer a neighboring track.
4. *Pattern cut*: Pattern cuts require that the lateral shower distribution of the energy associated with a track be consistent with an isolated, electromagnetically showering particle.<sup>28</sup> Tracks with narrow energy distributions are likely to be charged particles, and tracks with broad distributions are probable overlapping showers. If we define  $E_4$  as the energy of the maximum module and its three nearest neighbors, and  $E_{13}$  as the energy of the maximum and its twelve nearest and next nearest neighbors, the pattern cut requirement may be written:  $0.70 \leq E_4/E_{13} \leq 0.995$  and  $0.40 \leq E_{max}/E_4 \leq 0.980$ . This cut was developed primarily to remove charged particles,<sup>28</sup> which it does independently of the charged particle tracking system.

### C. Fitting Procedure

The number of  $\pi^0$  mesons from the  $D^* \rightarrow \pi^0 D$  cascade was calculated in two steps. First, the  $T_{\gamma\gamma}$ - $m_{\gamma\gamma}$  histogram was fit to extract the  $T_{\pi^0}$  spectrum. Then, the  $T_{\pi^0}$  spectrum from data on the  $\psi''(3772)$  resonance (below  $D^*$  threshold) was used to subtract the non-cascade  $\pi^0$  contribution.

The kinetic energy  $T_{\gamma\gamma} = E_{\gamma\gamma} - m_{\gamma\gamma}$  is a more appropriate variable than the total energy  $E_{\gamma\gamma}$  for two reasons. An  $E_{\gamma\gamma}$ - $m_{\gamma\gamma}$  histogram has a kinematical boundary  $E_{\gamma\gamma} \geq m_{\gamma\gamma}$ , which complicates the fitting procedure. In addition, the shifts in  $E_{\gamma\gamma}$  and  $m_{\gamma\gamma}$  due to energy measurement errors are correlated and cancel for small  $T_{\gamma\gamma}$ . Thus, the  $D^*$  signal stands out more sharply from the background.

The  $T_{\gamma\gamma}$ - $m_{\gamma\gamma}$  histograms were fit using a two-dimensional background sheet and independent gaussian peak functions to represent the  $\pi^0$  contributions to given  $T_{\gamma\gamma}$  slices. The peak parameters were smoothed values obtained by fitting independent slices of the histogram in fig. 7. The background sheet was parametrized by the basis functions  $f_i(m_{\gamma\gamma})g_j(T_{\gamma\gamma})$ , where  $f_i$ ,  $i=1,4$  and  $g_j$ ,  $j=1,5$  are Tschebycheff polynomials and  $g_6$  is the  $T_{\gamma\gamma}$  projection of the alternate event background discussed below. This final function assisted in reproducing the rise in the background in the low  $T_{\gamma\gamma}$  region.

Kinetic energy slices of the fit (for the entire 3.87–4.5 GeV dataset) in the cascade  $\pi^0$  signal region are shown in fig. 8, and the resulting  $T_{\pi^0}$  spectrum is shown in fig. 9(a). The same procedure yields the  $T_{\pi^0}$  spectra for the 14  $E_{c.m.}$  steps (see fig. 10). Note that these spectra are not acceptance corrected. The  $D^* \rightarrow \pi^0 D$  signal can be clearly seen in each of the  $E_{c.m.}$  steps.

As  $E_{c.m.}$  increases, so does the momentum of a  $D^*$  produced via two-body production. Thus, the maximum possible kinetic energy of a cascade  $\pi^0$  increases. In the energy region  $3.87 \leq E_{cm} \leq 4.2$  (GeV), the observed  $\pi^0$  cascade signal broadens in a manner consistent with two-body production of  $D^* \bar{D}$  and  $D^* \bar{D}^*$ . At higher center of mass energies, the width of the observed cascade signal is

narrower than can be explained by simple production of  $D$  and  $D^*$  mesons. This may be an indication that some of the observed  $D^*$  mesons are produced recoiling against or in decays of higher mass  $D$  mesons, which are thought to be produced in this energy region.<sup>29</sup> In addition, initial state radiation effects which alter the  $T_{\pi^0}$  spectrum become more important as the charm cross section begins to fall rapidly above 4.2 GeV. These data are not sufficient to untangle these effects and the  $D^*$  signal was not fit directly. Instead, the number of cascade  $\pi^0$  mesons was obtained by an extrapolative subtraction using the  $T_{\pi^0}$  spectrum from data below  $D^*$  threshold.

The uncorrected  $T_{\pi^0}$  spectrum obtained at the  $\psi''(3772)$  is displayed in fig. 9(b). The data in this region are roughly equal mixtures of light quark events and  $\psi''$  decays, which are predominantly  $D\bar{D}$ . Since the 3.87–4.5 GeV region contains similar proportions of light quark and  $D$  meson events, the  $\psi''(3772)$  is an appropriate place to model the non-cascade portion of the  $T_{\pi^0}$  spectrum. Note the absence of any structure in the low energy region of this spectrum.

A smooth representation of the shape of the  $T_{\pi^0}$  spectrum obtained at the  $\psi''(3772)$  was fit to the spectra observed above  $D^*$  threshold, excluding the  $D^*$  signal region ( $E_{cm}$  dependent), and extrapolated to  $T_{\pi^0} = 0$ . These non-cascade contributions are shown as the smooth curves in figures 9-10. The background contributions were then subtracted, and the signal region was integrated to obtain the number of  $D^*$  cascade  $\pi^0$  mesons.

A possible concern in this analysis is that the  $T_{\gamma\gamma}-m_{\gamma\gamma}$  background has non-smooth components that the fit is incapable of matching. This possibility was investigated through the alternate event background. The dominant features of the background in the region of the fit arise simply from the distributions of energies and angles of uncorrelated photons. These are modeled by combining photons from different events. These alternate event pairings are accumulated in such a way as to have the same normalization as the same-event histogram.

This method has proved useful for identifying inappropriate combinations of

cuts.<sup>8</sup> The alternate event spectrum for the photon cuts used in this analysis is shown in fig. 11. The smoothness of the alternate event spectrum indicates that these cuts yield a background shape sufficiently smooth to be fit by the methods employed.

#### D. Slow $\pi^0$ Detection Efficiency

Two Monte Carlo methods were used to determine the efficiency for reconstructing low energy  $\pi^0$  mesons. In the first method, the charmed meson Monte Carlo described in Sec. III was used to generate  $D^*\bar{D}$  and  $D^*\bar{D}^*$  events (half charged, half neutral). In the other method, the same Monte Carlo was used to generate the  $D^*$  cascade particles (including  $\gamma, \pi^\pm$ ), but the subsequent decays of the  $D$  mesons were not generated. The Monte Carlo crystal energies were merged into data events taken at the  $\psi''(3772)$ , and the events were re-analyzed.

The total event generation method has the advantage that all of the modeled events are  $D^*\bar{D}$  and  $D^*\bar{D}^*$ . However, these events are generally cleaner than real data events. In particular, the Monte Carlo does not generate a sufficient number of shower fluctuations from interacting hadronic particles, which can degrade the photons from  $\pi^0$  decay. The total event generation Monte Carlos were used to obtain the hadron selection efficiency for  $D^*$  events with observed cascade  $\pi^0$  mesons, and to correct for the probability that a photon converts in the beampipe or inner detector and is tracked by the inner detector.

The strength of the Monte Carlo merging technique is that it correctly models the hadronic environment in which the data  $\pi^0$  mesons are observed, except for a multiplicity correction discussed below. For this reason, the merging technique was used to obtain the  $\pi^0$  efficiency. There is the potential problem that the Monte Carlo  $\pi^0$  is not momentum correlated with the data event in which it is merged. Since the  $\pi^0$  mesons being modeled have low momenta, their momentum correlations with the rest of the event are small; moreover, for low energy  $\pi^0$  mesons the directions of the decay photons are less strongly correlated with the

direction of the  $\pi^0$ . A study of totally simulated Monte Carlo events indicated there was no measurable difference between the efficiency for finding a  $\pi^0$  in the event in which it was generated and the efficiency for finding it in an uncorrelated event into which it was merged.

The  $\pi^0$  efficiency obtained from Monte Carlo cascade  $\pi^0$  mesons merged into  $\psi''(3772)$  events must be corrected for multiplicity differences between the events in the 3.772 dataset and the data in the 3.87–4.5 GeV region. Not all of the events in the 3.772 sample are  $D\bar{D}$  events. Roughly half are light quark events, and about 15% are non-hadronic backgrounds.

The main determinant of the  $\pi^0$  detection efficiency in a given event is the *observed* multiplicity of the event with the  $\pi^0$  *removed*. An average track removes a fraction of the solid angle where a photon may be cleanly observed. The amount of “deadened” detector area grows with the *observed* multiplicity. The  $\pi^0$  detection efficiency as a function of  $\tilde{n}_{obs}$  is shown in fig. 12. The quantity  $\tilde{n}_{obs}$  is the number of tracks with energy greater than 20 MeV observed in the 3.772 event before the Monte Carlo  $\pi^0$  was merged. As may be seen, this is approximately a linear function of  $\tilde{n}_{obs}$ . The slope of the correction is roughly 2.4% per unit of observed multiplicity.

The number of data events with cascade  $\pi^0$  mesons having a given observed multiplicity was obtained by fitting the  $m_{\gamma\gamma}$  distribution for such events. (The efficiency can not be corrected simply for the average event multiplicity, since many of these events have no cascade pizero.) Also, if the  $\pi^0$  is observed, its photons must both be cleanly separated from other tracks; the total observed multiplicity including the  $\pi^0$  must be  $n_{obs} = \tilde{n}_{obs} + 2$ . The corrected efficiency was then obtained by weighting  $\epsilon(\tilde{n}_{obs})$  with the multiplicity distribution. The magnitude of this multiplicity correction is roughly 8% of the efficiency.

The statistics of the data were insufficient to correct each  $E_{cm}$  step separately. The efficiency for steps 2–14 (all above  $D^*\bar{D}^*$  threshold) was obtained by correcting the merged Monte Carlo efficiency using the method outlined above. The efficiency

for step 1 was then obtained using the difference in observed multiplicity between  $D^*\bar{D}$  and  $D^*\bar{D}^*$  Monte Carlo events. The final efficiencies for reconstructing a  $\pi^0$  are

$$\begin{aligned}\epsilon_{\pi^0} &= 0.34 \pm 0.01 & 3.870 \leq E_{cm} \leq 4.013 \text{ GeV} \\ \epsilon_{\pi^0} &= 0.32 \pm 0.01 & 4.013 \leq E_{cm} \leq 4.5 \text{ GeV}.\end{aligned}\tag{IV.1}$$

The errors above are the statistical errors from the number of events in the Monte Carlo. The estimated normalization error on the efficiency is  $\pm 10\%$  with an additional point to point systematic of 4% from uncertainties in the event multiplicity.

| Cuts (see text)                                     | average $\sigma(\text{slow } \pi^0)$ (nb) |
|---|---|
| solid angle cut                                     | $7.83 \pm 0.29$                           |
| solid angle, charged track cuts                     | $7.87 \pm 0.28$                           |
| solid angle, charged track, shower fluctuation cuts | $8.33 \pm 0.31$                           |
| solid angle, charged track, pattern cuts            | $7.95 \pm 0.25$                           |
| all cuts  | $8.02 \pm 0.28$                           |

*Table II.* Average slow  $\pi^0$  ( $T_{\pi^0} \leq 75$  MeV) cross sections obtained for different combinations of the cuts described in the text.

As a consistency check, the cross section for observing a  $\pi^0$  with less than 75 MeV kinetic energy was calculated using different combinations of the cuts outlined above. (See table II. Note that these cross sections are weighted over the entire energy range according to the luminosity profile of the Crystal Ball data.) The agreement between the values calculated using different cuts indicates that the Monte Carlo is correctly modeling the  $\pi^0$  reconstruction efficiencies.

## E. Results

Assuming isospin invariance (and neglecting the mass differences between the neutral and charged  $D$  mesons), the inclusive  $D^*$  cross section is calculated using the relation

$$\sigma(e^+e^- \rightarrow D^* + X) = \frac{N}{\epsilon_\pi \epsilon_{conv} \epsilon_{had} BR(D^* \rightarrow \pi^0 D) BR(\pi^0 \rightarrow \gamma\gamma) L} \quad [IV.2]$$

where  $N$  is the number of excess  $\pi^0$  mesons extracted using the method outlined above,  $L$  is the integrated luminosity,  $\epsilon_\pi$  the  $\pi^0$  reconstruction efficiency quoted above,  $\epsilon_{conv} = 0.98 \pm 0.01$  is the probability a  $\pi^0$  is not lost through conversion of its photons,  $\epsilon_{had} = 0.97 \pm 0.01$  is the acceptance for  $D^*$  events with observed cascade  $\pi^0$  mesons,  $BR(D^* \rightarrow \pi^0 D) = 0.428 \pm 0.052$  is the combined  $D^* \rightarrow \pi^0 D$  branching ratio,<sup>31</sup> and  $BR(\pi^0 \rightarrow \gamma\gamma) = 0.988$  is the  $\pi^0$  branching ratio into photons.<sup>30</sup>

Table III gives the results for the inclusive  $D^*$  cross sections. The first error quoted is the statistical error from the fitting procedure. The second error is a point to point systematic arising from changes in the event multiplicity (4%) and from a 25% uncertainty of the background subtracted under the  $D^*$  signal. As a constant normalization uncertainty, we estimate the error in the  $\pi^0$  efficiency to be 10%; the uncertainty in the cascade branching ratio uncertainty is  $\pm 12\%$ . Because of difficulties arising from the sizable error bars and from averaging over wide  $E_{cm}$  ranges, no radiative correction was performed. These results are plotted as  $R$  values in figure 13, where

$$R_{D^*} \equiv \frac{\sigma(e^+e^- \rightarrow D^* + X)}{\sigma_{\mu\mu}^0}. \quad [IV.3]$$

These results were calculated assuming that the same number of charged and neutral  $D^*$  mesons were produced. This assumption is slightly incorrect, due to small mass differences between the neutral and charged mesons. A precise



| $E_{cm}$ (Gev) | $\langle E_{cm} \rangle$ (Gev) | $\sigma(e^+e^- \rightarrow D^* + X)$ (nb) |
|----------------|--------------------------------|---|
| 3.870–4.013    | 3.949                          | $3.45 \pm 0.62 \pm 0.45$                  |
| 4.013–4.060    | 4.042                          | $16.96 \pm 0.94 \pm 0.87$                 |
| 4.060–4.102    | 4.080                          | $15.10 \pm 0.97 \pm 0.89$                 |
| 4.102–4.121    | 4.114                          | $14.75 \pm 0.89 \pm 0.89$                 |
| 4.121–4.129    | 4.124                          | $14.97 \pm 0.99 \pm 0.89$                 |
| 4.129–4.150    | 4.139                          | $12.66 \pm 0.91 \pm 0.83$                 |
| 4.150–4.174    | 4.161                          | $13.16 \pm 0.90 \pm 0.98$                 |
| 4.174–4.204    | 4.188                          | $15.25 \pm 0.84 \pm 0.99$                 |
| 4.204–4.240    | 4.216                          | $8.30 \pm 0.72 \pm 0.89$                  |
| 4.240–4.310    | 4.268                          | $6.03 \pm 0.57 \pm 0.78$                  |
| 4.310–4.360    | 4.339                          | $6.65 \pm 0.82 \pm 0.99$                  |
| 4.360–4.403    | 4.384                          | $10.76 \pm 0.93 \pm 1.29$                 |
| 4.403–4.428    | 4.419                          | $9.76 \pm 1.00 \pm 1.26$                  |
| 4.428–4.500    | 4.446                          | $9.60 \pm 1.02 \pm 1.15$                  |

Table III. Inclusive  $D^*$  cross sections

calculation of this correction requires knowledge of the threshold structure of the cross sections. From the distribution of data within the lowest two  $E_{cm}$  steps, it is estimated that the measured cross sections in the  $3.87 \leq E_{cm} \leq 4.013$ , and  $4.013 \leq E_{cm} \leq 4.06$  steps are 3%, and 5% too high.

These results are compared to previous measurements<sup>32,33</sup> in fig. 14. The Mark II collaboration measured the exclusive two-body  $D^*\bar{D}$ , and  $D^*\bar{D}^*$  cross sections between 3.9 and 4.3 GeV by fitting recoil mass spectra recoiling against reconstructed  $D$  mesons. The  $D$  mesons were reconstructed through the decays  $D^+ \rightarrow K^-\pi^+\pi^+$  and  $D^0 \rightarrow K^-\pi^+$ . The Mark II results plotted are combinations of their exclusive cross sections,  $\sigma(D^* + X) \equiv \sigma(D^*\bar{D}) + 2\sigma(D^*\bar{D}^*)$ , calculated

for this comparison.<sup>34</sup> The remaining point in fig. 14 is from a previous Crystal Ball measurement at 4.33 GeV.<sup>33</sup> All of these measurements are before radiative corrections. In relative terms, the radiative correction would enhance the dip in the cross section at 4.25 GeV and the peak at 4.03 GeV. (See fig. 15 for the general effect of the radiative correction.)

The inclusive  $D^*$  cross sections measured in this experiment are in good agreement with previous results. While the comparison with the Mark II values is quite good, it should be noted that the normalization of their measurements was determined by  $D$  branching ratios that are in disagreement with values obtained in subsequent experiments.<sup>35</sup>

Figure 15 compares the measured  $R(D^*)$  values with the prediction of the Eichten model.<sup>7</sup> The comparison is generally quite good. The normalization of the Eichten result partially reflects tuning the model to earlier experiments. These experiments tended to have higher  $R$  values than those measured in this experiment, particularly in the 4.4 GeV region. It should be noted that the masses for the  $F$  and  $F^*$  mesons used in the model were 2.035 and 2.135 GeV, in disagreement with present values.<sup>30</sup>

The  $R_{D^*}$  result may be combined with the  $R$  measurement of section III to calculate the average number of  $D^*$  mesons per charm event. In this calculation, the 3.67 data were used to estimate the contribution to  $R$  from light quark physics, and

$$\langle n_{D^*}(E_{cm}) \rangle = \frac{R_{D^*}(E_{cm})}{R(E_{cm}) - R(3.67)}. \quad [IV.4]$$

Since the  $D^*$  cross sections were not radiatively corrected, the  $R$  values used here were uncorrected, except for subtracting the radiative tails of the narrow vector resonances. The results of this calculation are displayed in figure 16. Recall that the first data point is below  $D^*\bar{D}^*$  threshold. These results indicate that charm events at these energies preferentially hadronize to events containing  $D^*$  mesons, leaving only small contributions from  $D\bar{D}$  production and states containing  $F$

mesons.

## V. CONCLUSIONS

We have measured total hadronic cross sections in  $e^+e^-$  annihilations at 3.67 GeV and center of mass energies between 3.87 and 4.5 GeV. The main features of the cross section in this region are a resonance at 4.03 GeV, a broader maximum at 4.4 GeV, and a broad shoulder near 4.16 GeV. A detailed plot of the cross section appears as fig. 4. This measurement agrees in broad details with previous measurements, with some disagreement over the structure in the 4.06–4.2 GeV region and the overall normalization.

The kinetic energy spectra of  $\pi^0$  mesons have been measured at energies between 3.87 and 4.5 GeV center of mass energy. A quasi-monochromatic, low energy peak ( $T_{\pi^0} \leq 50$  MeV) arising from  $D^* \rightarrow \pi^0 D$  cascade decays is observed. Using data taken at the  $\psi''(3772)$  to model the non-cascade contribution and assuming isospin invariance, the cross section for the process  $e^+e^- \rightarrow D^* + X$  is calculated from the excess number of low energy  $\pi^0$  mesons. This result extends previous experimental measurements and reasonably matches the predictions of the coupled channel model of Eichten *et al.* This result is combined with the total hadronic cross section measurements to calculate the average number of  $D^*$  mesons per charm event. The  $D^*$  multiplicity is approximately equal to 1 between  $D^*\bar{D}$  and  $D^*\bar{D}^*$  threshold, and 1.5–2 at higher energies. This indicates that charm events generally contain  $D^*$  mesons, and that  $D^*\bar{D}^*$  production is favored.

## APPENDIX A. RADIATIVE CORRECTIONS

The behavior of a cross-section in  $e^+e^-$  annihilation is usually dominated by the one-photon annihilation term, but contains contributions from all orders of quantum electrodynamics (QED). The contributions from diagrams with additional photon couplings are generically called radiative corrections. The lowest

order cross section displays the fundamental  $E_{cm}$  behavior, while the higher order terms are a convolution of the behavior at all energies. In addition, the size of the corrections can be heavily dependent on the details of the experimental apparatus and on the hadronic selection criteria. Unless the radiative contributions are understood and correctly treated in the acceptance calculation, the observed cross-sections from different experiments may not be directly comparable. This appendix describes the method used to extract a radiatively corrected cross-section by estimating and removing the higher order QED contributions.

The radiative correction is represented by  $1 + \delta$ , which multiplies the idealized cross-section to yield the observed cross-section.

$$\sigma(s) = (1 + \delta(s)) \sigma^0(s) \quad [A.1]$$

In this experiment, only first order, initial state corrections were performed. Because of the presence of the hadronic interaction, the final state corrections are complicated and model-dependent. Fortunately, they are small due to the KNL cancellations.<sup>22</sup>

Figure 17 shows the lowest order diagram, in addition to the diagrams which contribute in the next to leading order. The radiative correction may be similarly decomposed:

$$\delta = \delta_e + \delta_\mu + \delta_\tau + \delta_{had} + \delta_{vert} + \delta_\gamma. \quad [A.2]$$

The first four terms represent the vacuum polarization terms followed by the initial state vertex correction and the bremsstrahlung term. The diagrams that contain virtual photons contribute in lowest order only by interfering with the non-radiative amplitude and are independent of the detector acceptance. The bremsstrahlung diagrams, which contain a real photon radiated from the initial electron or positron, contribute directly. Because the kinematics of the  $e^+e^-$  pair is altered, these corrections depend on the apparatus and selection criteria, and on the hadronic cross-section at lower energies.

The vacuum polarization contributions to the radiative correction arise from inserting virtual states into the propagator of the annihilation photon. These states must have the quantum numbers of the photon, and the different polarization terms represent contributions from  $e^+e^-$ ,  $\mu^+\mu^-$ ,  $\tau^+\tau^-$ , and quark-antiquark pair loops. The leptonic terms have been calculated:<sup>36,37</sup>

$$\delta_i = \frac{2\alpha}{\pi} \left\{ \frac{(2+r)\sqrt{1-r}}{6} \ln \left[ \frac{1+\sqrt{1-r}}{1-\sqrt{1-r}} \right] - \frac{5}{9} - \frac{r}{3} \right\} \quad i = e, \mu, \tau \quad [A.3]$$

$$r = \frac{4m_i^2}{s}$$

where  $\alpha$  is the fine-structure constant and  $s = E_{cm}^2$ . For the electron and muon terms,  $r \ll 1$  and the expression reduces to

$$\delta_i = \frac{2\alpha}{\pi} \left[ \frac{1}{3} \ln \left( \frac{s}{m_i^2} \right) - \frac{5}{9} \right] \quad i = e, \mu. \quad [A.4]$$

The hadronic vacuum polarization term may be related to the total hadronic cross-section through a dispersion relation<sup>38</sup>

$$\delta_{had} = -\frac{s}{2\pi^2\alpha} \int_{4m_\pi^2}^{\infty} \frac{\sigma_{had}^0(s')}{s' - s} ds' = -\frac{2\alpha s}{3\pi} \int_{4m_\pi^2}^{\infty} \frac{R(s')}{s'(s' - s)} ds'. \quad [A.5]$$

Note that this term requires knowledge of the cross-section at all energies. Following Berends and Komen, this integral was calculated in pieces. The contributions from the narrow vector resonances were done analytically. Next,  $R$  was assumed to be constant above some value  $s = s_1$ . The integral is insensitive to the value of  $R$  at high energies. After separation of the principal part, the remainder of the integral was done numerically, using  $R$  values from this and

other experiments

$$\begin{aligned}
\delta_{had}(s) = & \frac{6s}{\alpha} \sum_j \frac{\Gamma_{ee,j}}{M_j} \frac{s - M_j^2 - \Gamma_{tot,j}^2}{M_j^2 \Gamma_{tot,j}^2 + (s - M_j^2)^2} \\
& + \frac{2\alpha}{3\pi} \tilde{R}(s_1) \ln \left| \frac{s_1 - s}{s_1} \right| - \frac{2\alpha}{3\pi} \tilde{R}(s) \ln \left| \frac{s_1 - s}{4m_\pi^2 - s} \right| \\
& - \frac{2\alpha}{3\pi} \int_{4m_\pi^2}^{s_1} \frac{1}{s' - s} \left[ \frac{s}{s'} \tilde{R}(s') - \tilde{R}(s) \right] ds'.
\end{aligned} \tag{A.6}$$

The function  $\tilde{R}$  is  $R$  with the narrow resonances removed.

The isolated vertex term has an infrared divergence, which cancels a corresponding soft photon divergence in the bremsstrahlung term. The finite remainder<sup>36</sup> is

$$\delta_{vert} = \frac{2\alpha}{\pi} \left[ \frac{3}{4} \ln \left( \frac{s}{m_e^2} \right) - 1 + \frac{\pi^2}{6} \right]. \tag{A.7}$$

The bremsstrahlung term accounts for the portion of the cross-section arising from the radiation of real photons by the initial state charged particles. Since this radiation lowers the  $E_{cm}$  of the  $e^+e^-$  pair, the bremsstrahlung term depends on the hadronic cross-section at lower energies. The contribution<sup>36</sup> from events with a radiative photon of energy  $k$  is

$$\begin{aligned}
d\sigma_{brem} &= F(s, k) dk \\
F(s, k) &= t \left( 1 - \frac{k}{E_{beam}} + \frac{k^2}{2E_{beam}^2} \right) \sigma^0(s') \frac{1}{k} \\
t &= \frac{2\alpha}{\pi} \left[ \ln \left( \frac{s}{m_e^2} \right) - 1 \right]
\end{aligned} \tag{A.8}$$

where  $s' = s \left( 1 - \frac{k}{E_{beam}} \right)$  is  $s$  of the  $e^+e^-$  system after radiation. The quantity  $t$ , called the equivalent radiator, is roughly 0.08 in the energy region considered here.

Note that  $F(s, k) \sim \frac{1}{k}$  for small  $k$ , and thus  $\sigma_{brem}$  is logarithmically divergent. This piece cancels the infrared divergence of the vertex correction. Including higher order corrections,<sup>39</sup>  $F(s, k) \sim k^{t-1}$ . Thus, the form of the bremsstrahlung spectrum used was  $F(s, x) = t x^{t-1} (1 - x + x^2/2) \sigma^0(s')$ , where  $x = k/E_{beam}$ . Dividing by  $\sigma^0(s)$  and integrating,

$$\delta_\gamma = t \int_0^{x_{max}} x^{t-1} \left[ \left( 1 - x + \frac{x^2}{2} \right) \frac{1}{1-x} \frac{R(s')}{R(s)} - 1 \right] dx + x_{max}^t - 1. \quad [A.9]$$

The allowed values of  $k$  range from 0 to  $k_{max}/E_{beam} = 1 - 4m_\pi^2/s$ , corresponding to radiation to the lowest mass hadronic state.

Because the fractions of radiative hadronic events that appear hadronic or beam-gas-like depends on the energy of the radiative photon, it is more practical to slightly recast the results above. Let  $\epsilon(k)$  and  $b_{had}(k)$  be the fractions of events with radiative photons of energy  $k$  that contribute to  $N_{sel}$  and  $N_{bgcut}$ , respectively. Then, in the derivation of eq. [III.5] in Sec. III, we may replace  $\bar{\epsilon}^{eff} N_{had}$  by

$$L \cdot \epsilon^{eff}(0) \sigma^0(1 + \delta_{obs}),$$

where

$$\delta_{obs} = \delta_e + \delta_\mu + \delta_\tau + \delta_{had} + \delta_{vert} + \delta_{\gamma obs}, \quad [A.10]$$

$$\delta_{\gamma obs} = t \int_0^{x_{max}} x^{t-1} \left[ \left( 1 - x + \frac{x^2}{2} \right) \frac{\epsilon_{rel}^{eff}(x)}{1-x} \frac{R(s')}{R(s)} - 1 \right] dx + x_{max}^t - 1 \quad [A.11]$$

and

$$\epsilon_{rel}^{eff}(x) \equiv \frac{\epsilon(x) - h_{bg} b_{had}(x)}{\epsilon(0) - h_{bg} b_{had}(0)}. \quad [A.12]$$

Recasting the product of the efficiency and the radiative correction in this form, the radiative effects in  $\bar{\epsilon}^{eff}$  are more explicitly displayed. The net effect is the replacement

$$\bar{\epsilon}^{eff}(1 + \delta) \rightarrow \epsilon^{eff}(0) (1 + \delta_{obs}).$$

For computational reasons, the contributions from radiation to the narrow resonances are separated and done analytically.<sup>40</sup> Substituting

$$\sigma_{res}^j = \frac{12\pi\Gamma_{ee,j}\Gamma_{had,j}}{(s - M_j^2)^2 + \Gamma_{tot,j}^2 M_j^2} \quad [A.13]$$

into the expression for  $\sigma_{brem}$ , the radiative tail to a narrow resonance is

$$\sigma_{tail}^j = t \frac{12\pi^2\Gamma_{ee,j}\Gamma_{had,j}}{\Gamma_{tot,j}M_j s} \left(\frac{k_{res}}{E_b}\right)^{t-1} \left[1 - \frac{k_{res}}{E_b} + \frac{k_{res}^2}{2E_b^2}\right] \quad [A.14]$$

$$k_{res} = E_b \left(1 - \frac{M_j^2}{s}\right)$$

Thus, the equation for  $R$  becomes

$$R = \frac{N_{sel} - h_{bg}N_{bgcut} - \sum_i (h_i - h_{bg}b_i) n_i - \sum_j L\epsilon_{tail,j}^{eff}\sigma_{tail}^j}{L\sigma_{\mu\mu}^0\epsilon^{eff}(0)(1 + \delta_{obs})}. \quad [A.15]$$

## B. Implementation

The radiative correction,  $1 + \delta_{obs}$ , depends on both the effective hadronic acceptance of radiative events, and the hadronic cross-section at all energies.

The relative radiative acceptance function,  $\epsilon_{rel}^{eff}(k)$ , was determined from the various hadronic Monte Carlo simulations discussed in section III. To a good approximation, this relative acceptance was independent of the model and was a simple function of  $x = k/E_{beam}$ . Figure 18 shows this relative acceptance function. In removing the radiative tails, it was assumed that this same  $k$  dependence applied to the acceptance for radiative resonance events.

The function  $\tilde{R}(E_{cm})$  used for calculating the radiative corrections contains results from other experiments matched onto the data from this experiment in the region  $3.67 \leq E_{cm} \leq 4.5$  GeV. Thus, equation [A.15] provides an



integral equation for  $R$  and was solved using an iterative technique. Since the bremsstrahlung correction magnifies any fluctuation in  $R$ , the  $\tilde{R}$  ( $R$  with narrow resonances removed) values were smoothed before calculating the radiative corrections. Initially, the non-radiatively corrected  $R$  values were used to calculate  $\delta_{obs}$  and perform the first approximation to the radiative correction. These corrected values were smoothed and used to calculate a second approximation, etc. This process rapidly converges.

In summary, the radiative correction is comprised of three qualitatively different pieces. The vertex correction and leptonic vacuum polarization terms do not depend on the shape of the cross section and are detector independent. They vary slowly over the energy range of this experiment, and their sum is roughly 10%. The hadronic vacuum polarization correction can be expressed as an integral involving the hadronic cross section at all energies, but is particularly dependent on the shape of  $R$  at nearby energies. This correction varies from 1.5–2.% in this energy region. The final piece of the radiative correction, the bremsstrahlung term, depends upon  $R$  at lower energies and upon the acceptance for radiative events. This term strongly reflects the shape of the cross section and varies between –17% and 0% with an additional 0.1–0.25 units of  $R$  from the tails of the narrow vector resonances. Because of the radiative effects in the acceptance, it is more useful to quote the product of the efficiency and radiative corrections  $\bar{\epsilon}^{eff}(1+\delta) = \epsilon^{eff}(0)(1+\delta_{obs})$ . This total correction, including the tails of the narrow resonances varies between 0.89 and 1.05.

## ACKNOWLEDGMENTS

We gratefully acknowledge the efforts of A. Baumgarten and J. Broeder (SLAC) and B. Beron, E. B. Hughes, and R. Parks (High Energy Physics Laboratory, Stanford University), as well as those of the linac and SPEAR staff at SLAC. This work was supported in part by the Department of Energy under contracts DE-AC03-76SF00515 (SLAC), DE-AC02-76ER03064 (Harvard),

and DE-AC03-81ER40050 (CIT); by the National Science Foundation contracts PHY81-07396 (HEPL), PHY79-16461 (Princeton), and PHY75-22980 (CIT); by the NATO Fellowship (HK), the Chaim Weizmann Fellowship (FP) and the Sloan Foundation (TB).

- (a) Present address: Dept. of Physics, Lawrence Livermore Laboratory, P.O. 808 Livermore, CA.
- (b) Present address: CERN, EP Division, 1211 Geneva 23, Switzerland.
- (c) Present address: Universität Dortmund, Dortmund, Federal Republic of Germany.
- (d) Present address: Universität Würzburg, Würzburg, Federal Republic of Germany.
- (e) Present address: EMR Photoelectric, P.O. Box 44, Princeton, NJ 08540.
- (f) Present address: VIDCO Inc., Cupertino, California 95014.
- (g) Present address: SSC Central Design Group, Lawrence Berkeley Laboratory, Berkeley, CA.
- (h) Present address: Brown University, Providence RI 02912.
- (i) Present address: Institute of High Energy Physics, Academia Sinica, Beijing, People's Republic of China.
- (j) Present address: Hermann Distel Strasse 28, D-2050 Hamburg 80, Federal Republic of Germany.
- (k) Present address: III Phys. Inst. der Techn. Hochschule, Aachen, Federal Republic of Germany.
- (l) Present address: University of Cape Town, Physics Department, Cape Town, South Africa.
- (m) Present address: Physics Department, University of Washington, Seattle, Washington 98195.
- (n) Present address: SCIPP, University of California at Santa Cruz, Santa Cruz, California 95064.
- (o) Present address: Massachusetts Institute of Technology, Laboratory for Nuclear Science, Cambridge, MA 02139.
- (p) Present address: 830 Tulane Drive, Mountain View, California 94040.

- (q) Present address: IntelliCorp, Mountain View, California 94040.
- (r) Present address: Max Planck Institute for Physics and Astrophysics, D-8000 Munich 40, Federal Republic of Germany.
- (s) Present address: Enrico Fermi Institute, University of Chicago, Chicago, Illinois 60637.

## REFERENCES

- 1) J. D. Bjorken, S. L. Glashow, *Phys. Lett.* 11, 1964, 255.
- 2) S. L. Glashow, J. Iliopoulos, L. Maiani, *Phys. Rev. D* 2, 1970, 1285.
- 3) T. Appelquist and H. D. Politzer, *Phys. Rev. Lett.* 34, 1975, 43.
- 4) J. E. Augustin *et al.*, *Phys. Rev. Lett.* 33, 1974, 1406.
- 5) G. S. Abrams *et al.*, *Phys. Rev. Lett.* 33, 1974, 1453.
- 6) P. A. Rapidis *et al.*, *Phys. Rev. Lett.* 39, 1977, 526; W. Bacino *et al.*, *Phys. Rev. Lett.* 40, 1978, 671; R. H. Schindler *et al.*, *Phys. Rev. D* 21, 1980, 2716.
- 7) E. Eichten *et al.*, *Phys. Rev. D* 21, 1980, 203.
- 8) These analyses are described in more detail in A. Osterheld, Ph.D. thesis, Stanford University, 1985, and SLAC Report 304.
- 9) M. Oreglia, Ph.D. thesis, Stanford University, 1980, and SLAC Report 236; M. Oreglia *et al.*, *Phys. Rev. D* 25, 1982, 2259.
- 10) J. Gaiser *et al.*, *IEEE Trans. Nucl. Sci.*, NS-26 No. 1, 1979, 173.
- 11) C. Edwards *et al.*, SLAC-PUB 3030.
- 12) Minor triangles are groups of 9 crystals, and major triangles are groups of 36 crystals. See ref. 9 for more details.
- 13) R. L. Ford and W. R. Nelson, *The EGS Code System*, SLAC-0210, June 1978.

- 14) Oak Ridge National Laboratory Report CCC-178, August, 1977.
- 15) G. Feldman, SLAC PUB 2068, 1977.
- 16) C. Quigg and J. Rosner, Phys. Rev. D17 (1978) 239.
- 17) R. Partridge, Ph.D. thesis, Cal. Inst. of Tech., 1984 (unpublished).
- 18) T. Sjöstrand, Comp. Phys. Comm. 27, 1982, 243.
- 19) F. A. Berends and R. Kleiss, Nucl. Phys. B228, 1983, 537;  
       F. A. Berends and R. Kleiss, Nucl. Phys. B186, 1981, 22;  
       F. A. Berends and R. Kleiss, Nucl. Phys. B177, 1981, 237;  
       F. A. Berends, R. Kleiss, S. Jadach, Z. Was, Acta Phys. Polon. B14, 1983,  
       413.
- 20) S. Brodsky *et al.*, Phys. Rev. D4, 1971, 1532.
- 21) C. Berger *et al.*, Phys. Lett. 89B, 1979, 120;  
       C. Berger *et al.*, Phys. Lett. 89B, 99B, 1980, 287.
- 22) T. D. Lee, M. Nauenberg, Phys. Rev. B133, 1964, 1549; T. Kinoshita, J.  
       Math. Phys. 3, 1962, 650.
- 23) Y. S. Tsai, SLAC-PUB 3129, 1983; E. A. Kuraev and V. S. Fadin, Sov.  
       Journ. Nucl. Phys. 41, 466, 1985.
- 24) J. Burmeister *et al.*, Phys. Lett. 66B, 1977, 395.
- 25) R. Brandelik *et al.*, Phys Lett 76B, 1978, 361.
- 26) J. L. Siegrist *et al.*, Phys. Rev. D26, 1982, 969.
- 27) The track energy is estimated by the sum of the energies of the central  
       module of the shower and its 12 nearest neighbors. Energy leakage and  
       position corrections are applied.
- 28) J. Gaiser, Ph.D. thesis, Stanford University, 1982, and SLAC Report 255.
- 29) H. Albrecht *et al.*, Phys. Lett. 153B, 1985, 343.

- 30) Particle Data Group, Phys. Lett. 170B, 1986
- 31) The branching ratios are from ref. 30. The error on the combined  $\pi^0$  branching ratio assumes that the errors are uncorrelated.
- 32) M. W. Coles *et al.*, Phys. Rev. D26, 1982, 2190.
- 33) R. Horisberger, Ph.D. thesis, Stanford University, 1984, and SLAC Report 266.
- 34) The values from their isotropic fits were used for this comparison.
- 35) R. M. Baltrusaitis *et al.*, Phys. Rev. Lett. 56, 2140 (1986). Reference 32 used 0.03 for the  $D^0 \rightarrow K^- \pi^+$  branching ratio, and 0.063 for the  $D^+ \rightarrow K^- \pi^+ \pi^+$  branching ratio. The values now quoted in ref. 30 are 0.054 and 0.114, respectively.
- 36) G. Bonneau and F. Martin, Nucl. Phys. B27, 1971, 141.
- 37) F. A. Berends and R. Kleiss, Nucl. Phys. B178, 1981, 141.
- 38) F. A. Berends and G. J. Komen, Phys. Lett. 63B, 1976, 432.
- 39) D. R. Yennie, S. C. Frautschi, and H. Suura, Ann. Phys. 12, 379 (1961).
- 40) J. D. Jackson, and D. L. Scharre, Nucl. Instr. and Methods 128, 1975, 13.

## FIGURE CAPTIONS

- 1. The Crystal Ball detector components.
- 2. Distributions of beam timing for (a) all events, and (b) hadron sample, and of  $E_{visible}/E_{cm}$  for (c) all events, and (d) hadron sample.
- 3. The initial iteration of the radiative correction. The curve is a smoothed representation of approximate  $R$  values calculated as if no radiative effects were present, and the points are  $R$  values obtained by using this smooth curve to calculate the radiative corrections.

4. Total hadronic cross sections normalized to the point-like cross section. The errors include the statistical errors from counting the number of hadron and beam-gas candidates, as well as the estimated systematic error from the beam-gas subtraction.
5. A comparison of  $R$  values from this analysis to previous  $R$  measurements in the 3.5 to 5.0 GeV range.
6. Summary of the decay modes and branching ratios of the of the low-lying, non-strange, charmed mesons.
7. Histogram of kinetic energy—invariant mass combinations for all pairs of photon candidates in an event. All data with  $3.87 \leq E_{c.m.} \leq 4.5$  GeV is included.
8. Slices of the histogram in fig. 7 parallel to the invariant mass axis. The  $T_{\pi^0}$  limits of the slices are given in MeV. The smooth curves are corresponding slices of the fit and background functions described in the text.
9. Distributions of  $\pi^0$  kinetic energies for (a) the entire dataset, and (b) data at the  $\psi''(3.772)$ . No acceptance corrections have been performed. The shape of the smooth curves is derived from the  $\psi''(3.772)$  spectrum. The normalization of the curve in (a) is obtained by fitting the portion of the spectrum with  $T_{\pi^0} > 50$  MeV.
10. Uncorrected  $T_{\pi^0}$  spectra for the 14  $E_{c.m.}$  steps, overlaid with the estimated non-cascade contribution.
11. Uncorrected  $T_{\pi^0}$  spectrum obtained from pairing photon candidates from alternate events, using the entire dataset. These pairings cannot reconstruct real  $\pi^0$  mesons and model the shape of the two dimensional background in fig. 7.
12. The  $\pi^0$  reconstruction efficiency as a function of  $\tilde{n}_{obs}$ , the event multiplicity that would be observed if the  $\pi^0$  were removed.

13. Inclusive  $D^*$  cross sections normalized to point-like cross sections. The plotted errors are the statistical errors from the fits.
14. A comparison of  $R_{D^*}$  with previous measurements. The diamond points are from ref. 32, and the square from ref. 33.
15. A comparison of  $R_{D^*}$  with the predictions of the coupled channel model. The curve is the lowest order model prediction and the diamond points have the radiative corrections added. They have also been binned for comparison with the data. (See note in text about masses of  $F$ , and  $F^*$  mesons.)
16. The average  $D^*$  multiplicity per charm event.
17. Generic first order, initial state radiative correction diagrams: a) lowest order hadronic cross section; b) vertex correction; c) vacuum polarization corrections; d) bremsstrahlung correction.
18. Acceptance of radiative hadronic events, relative to non-radiative hadronic acceptance.

# THE CRYSTAL BALL EXPERIMENT

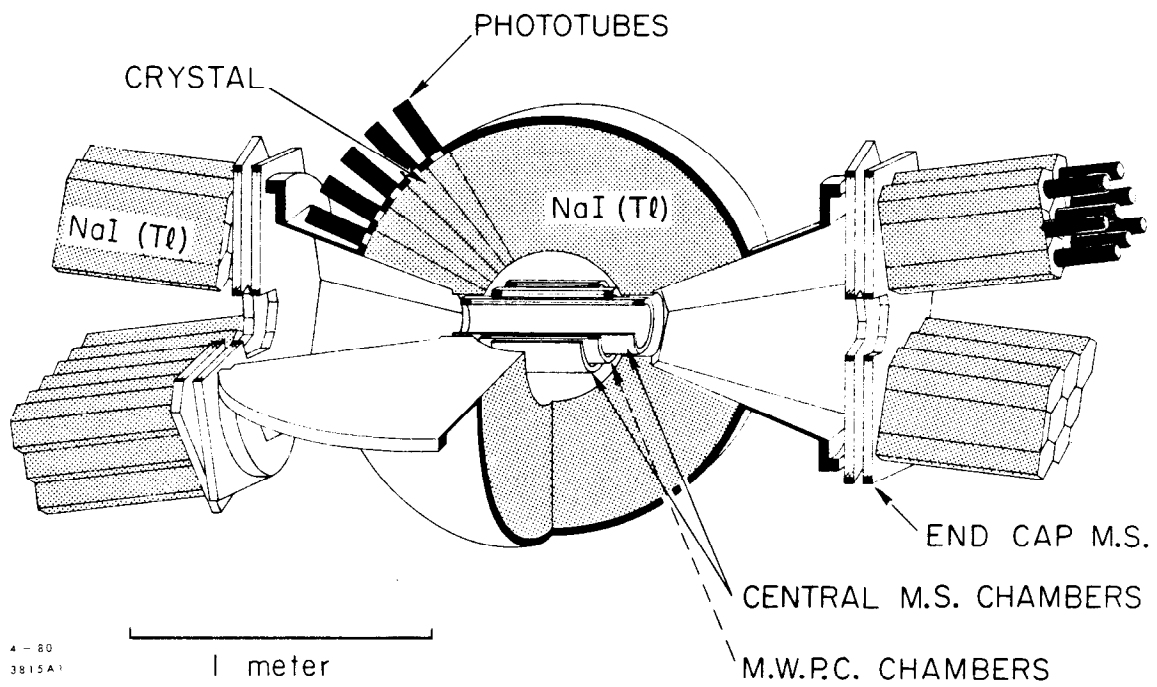
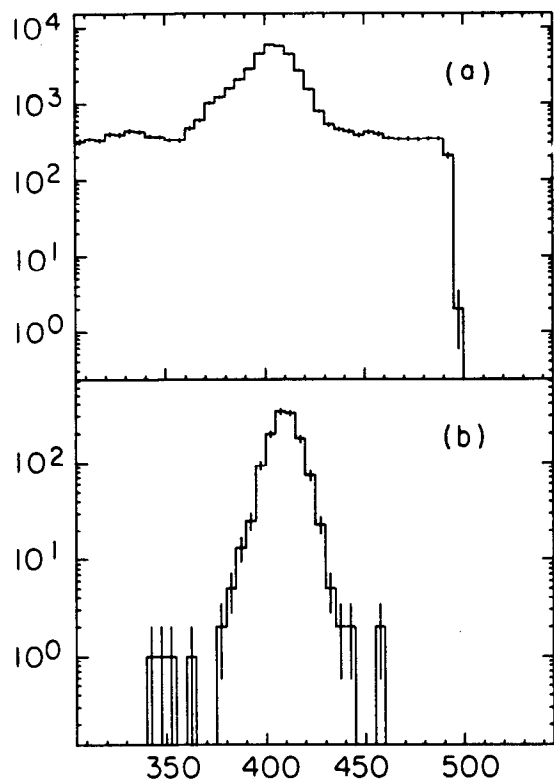
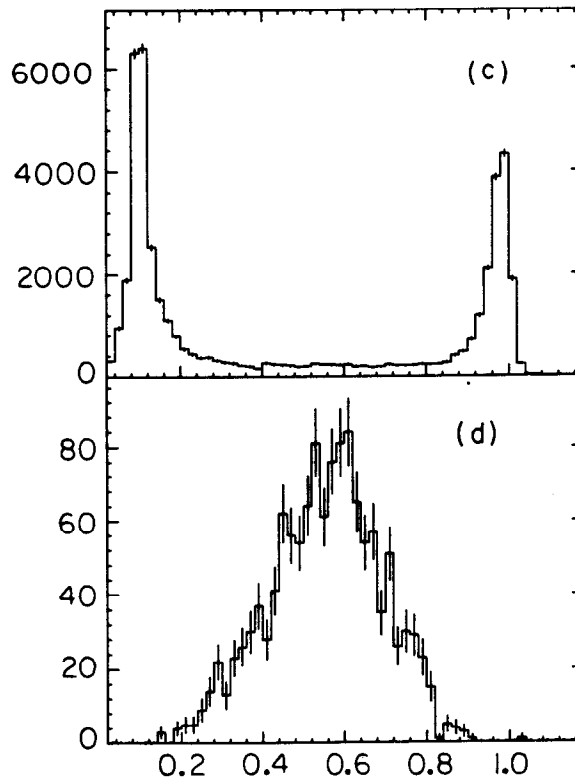


Fig. 1





11-86



5587A4

Fig. 2

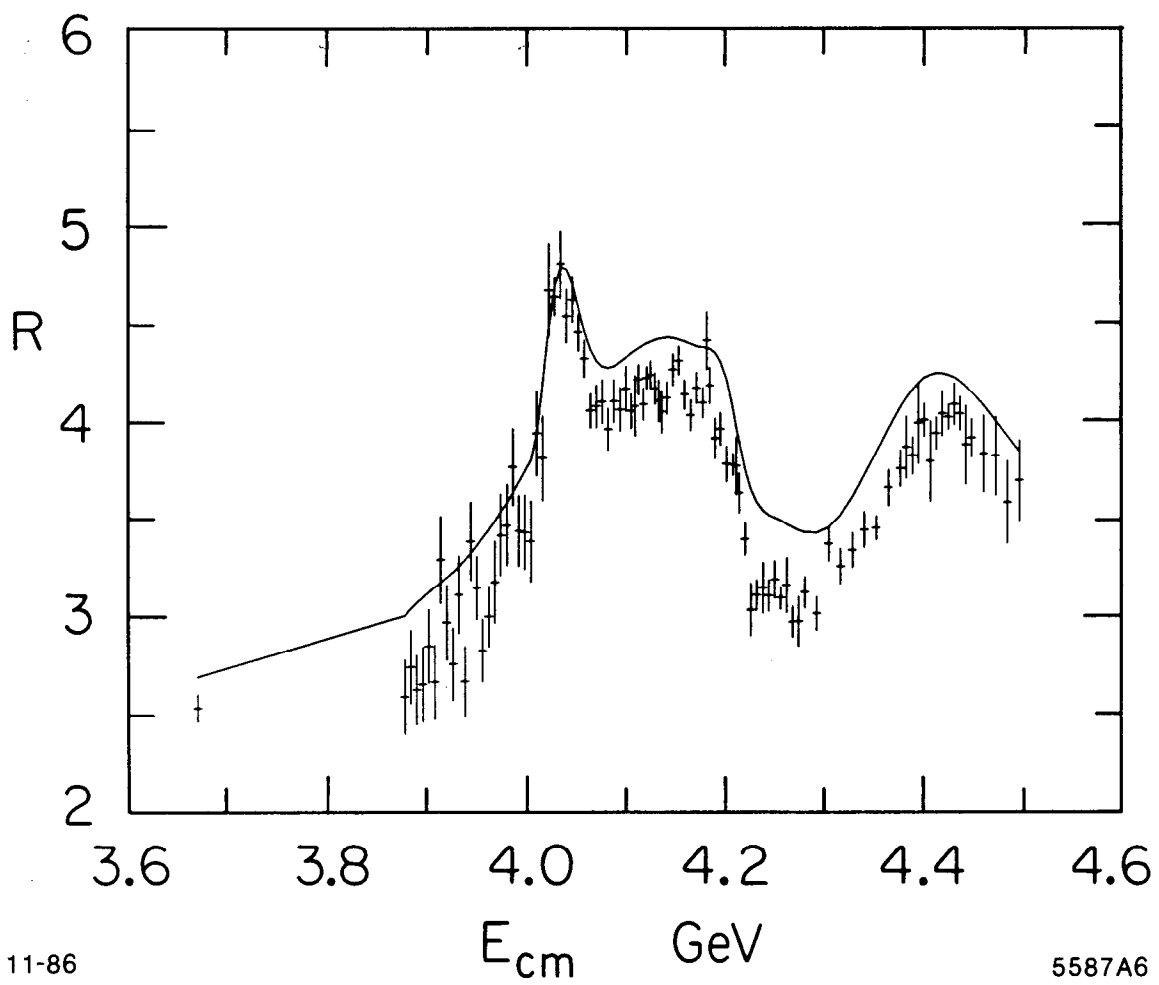
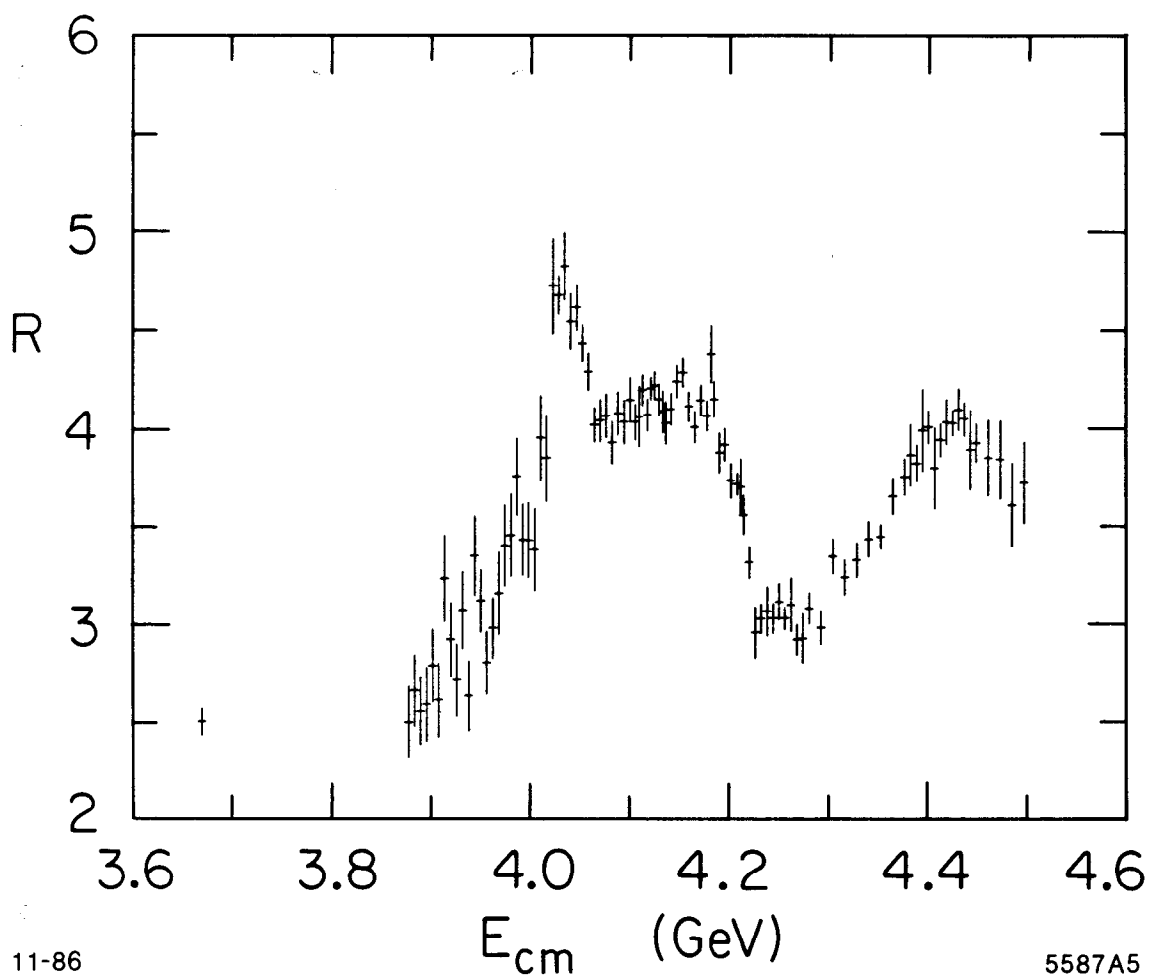


Fig. 3



11-86

5587A5

Fig. 4

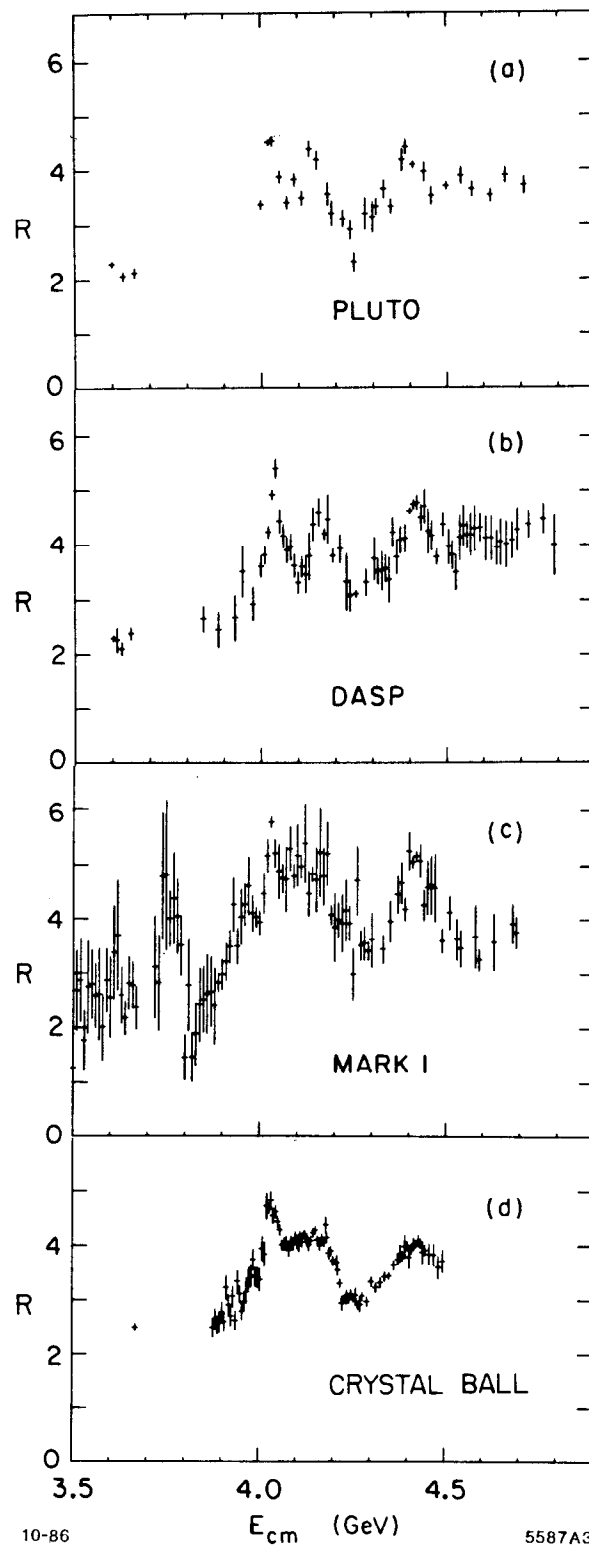
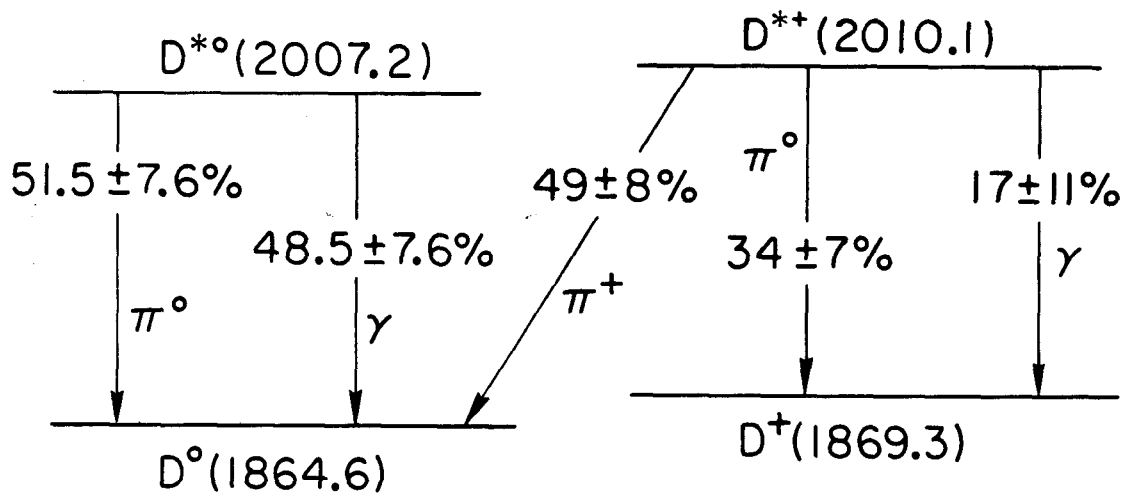


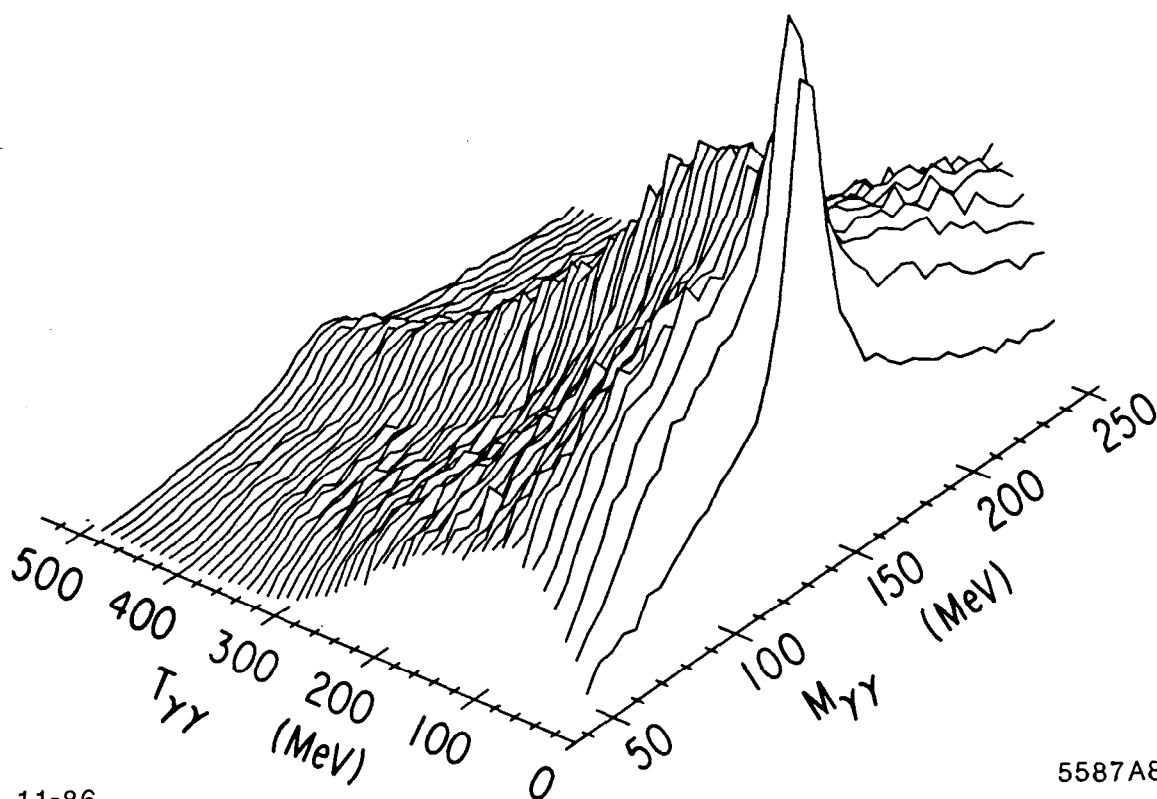
Fig. 5



11-86

5587A7

Fig. 6



11-86

5587A8

Fig. 7

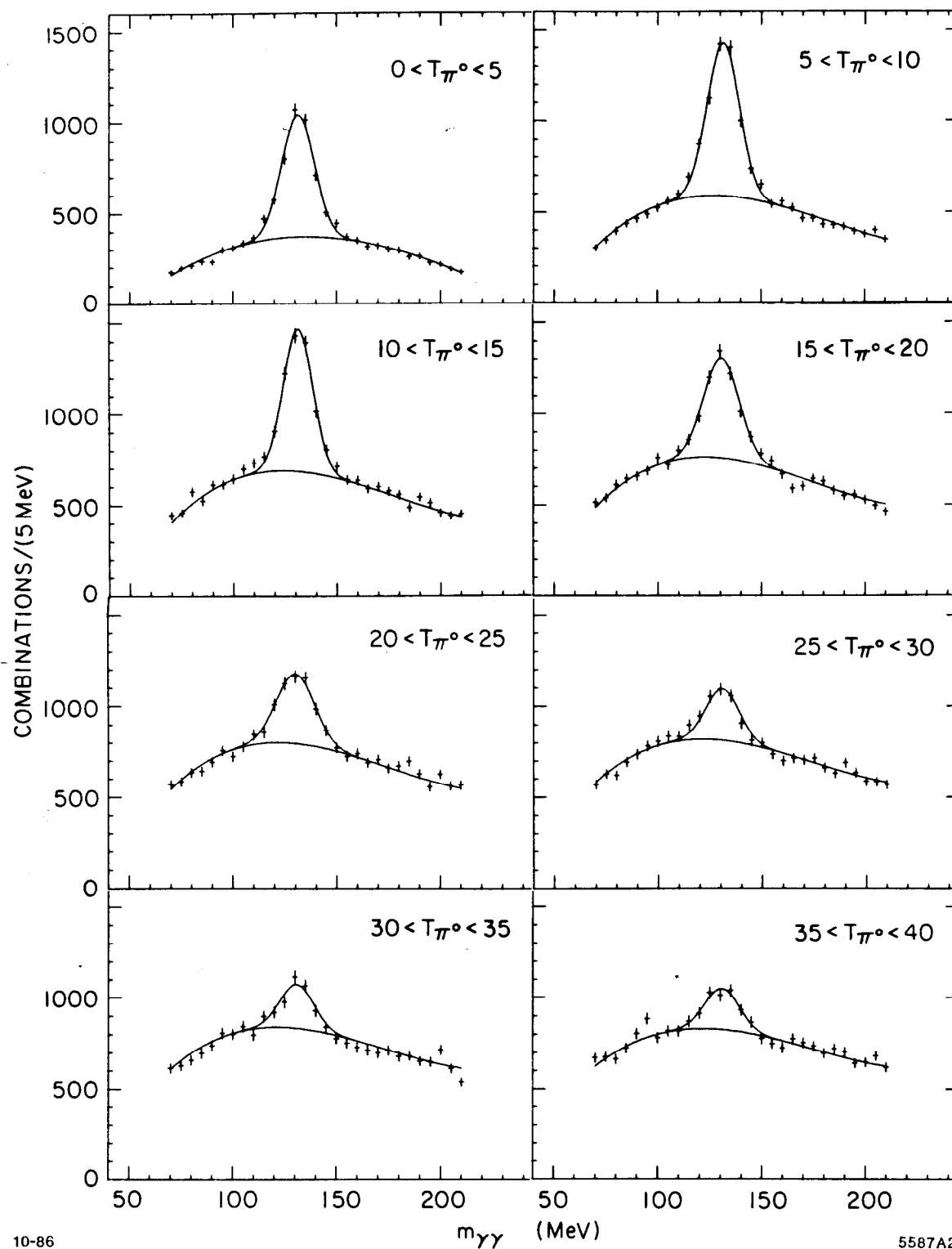
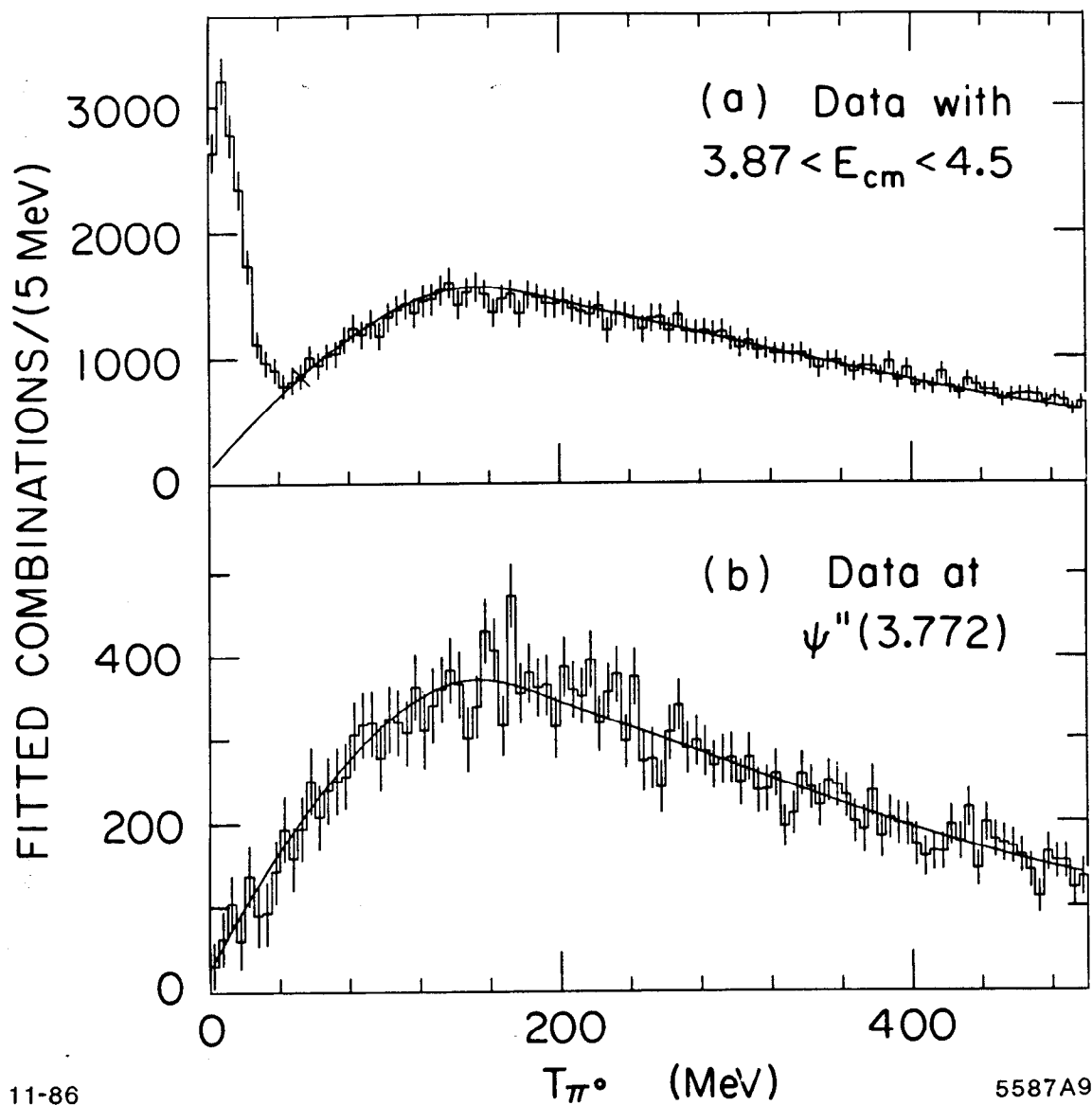


Fig. 8



11-86

5587A9

Fig. 9

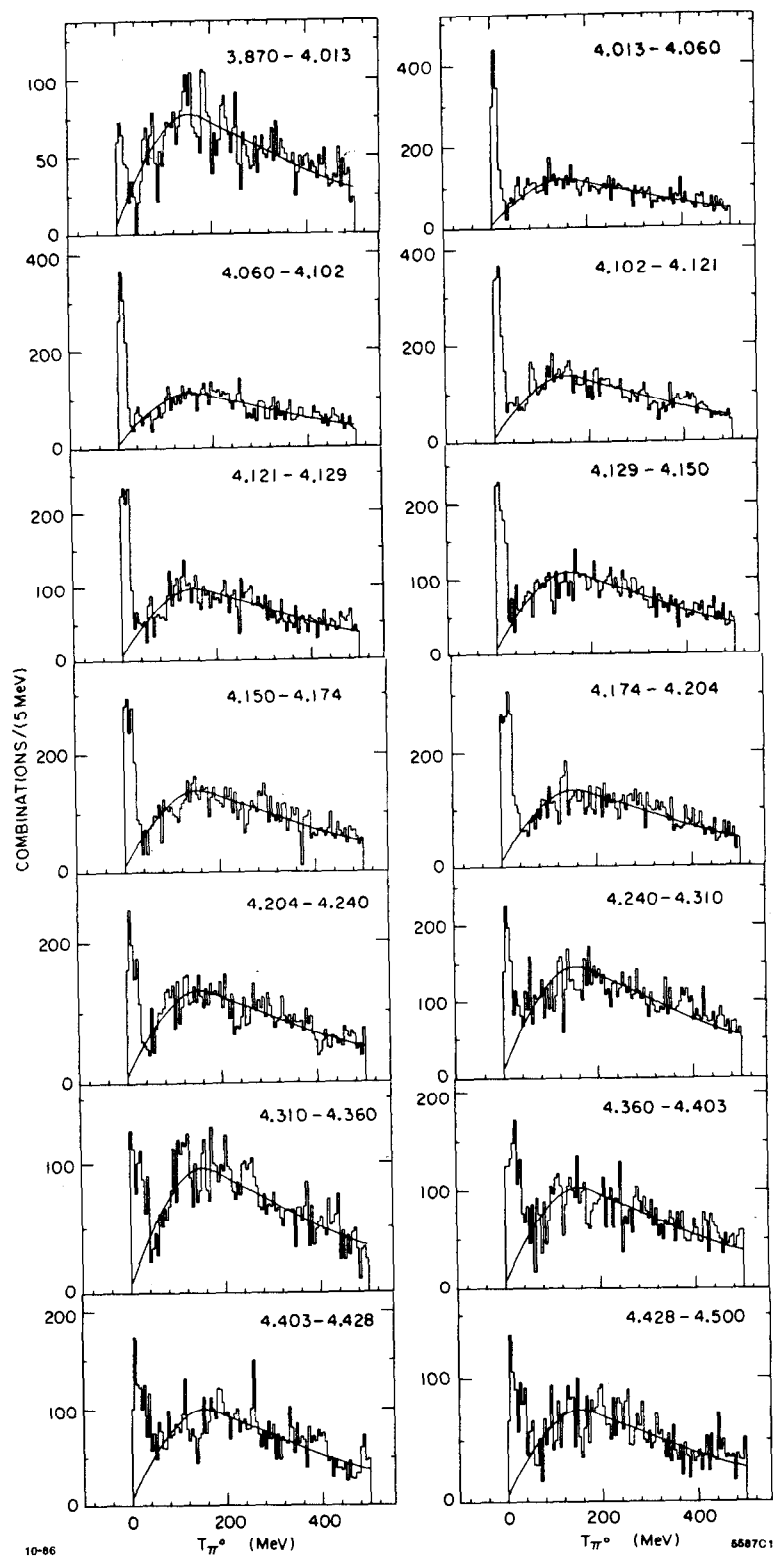


Fig. 10



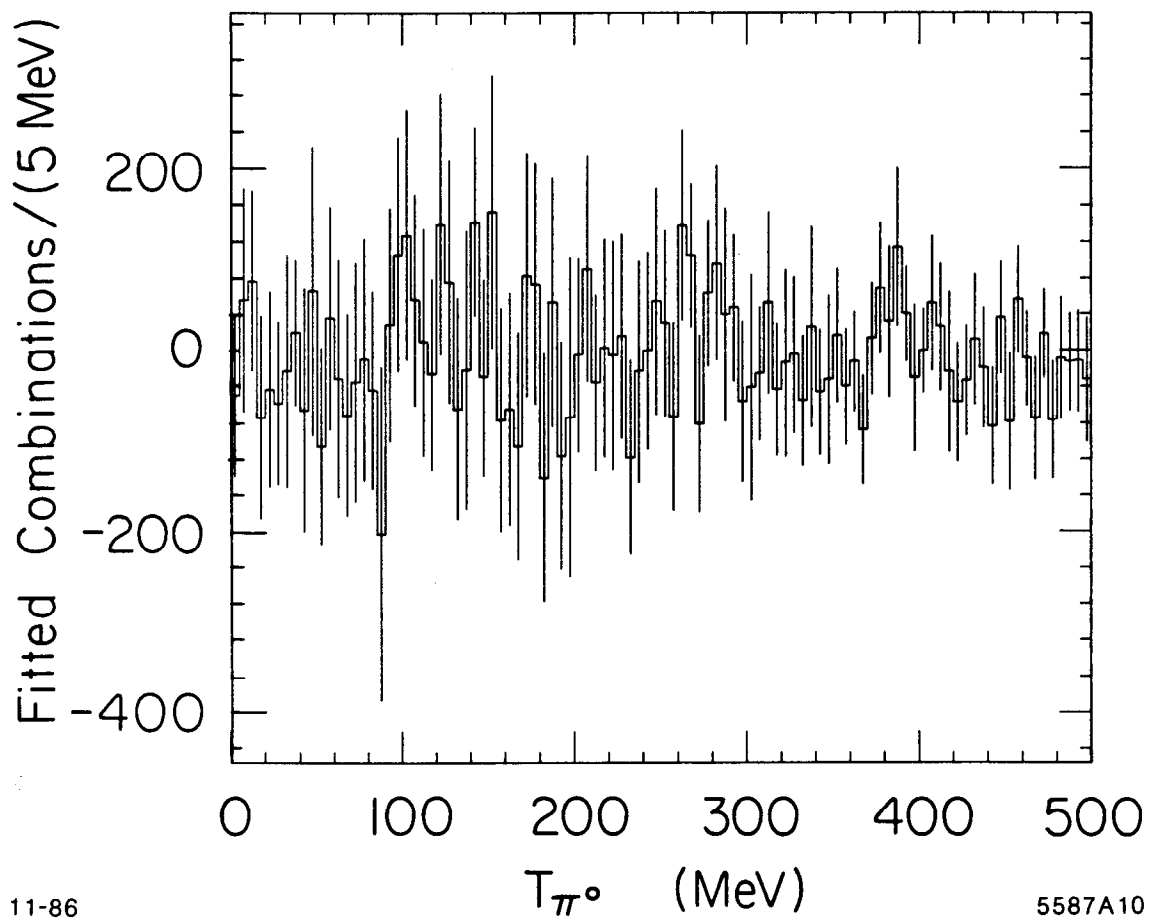
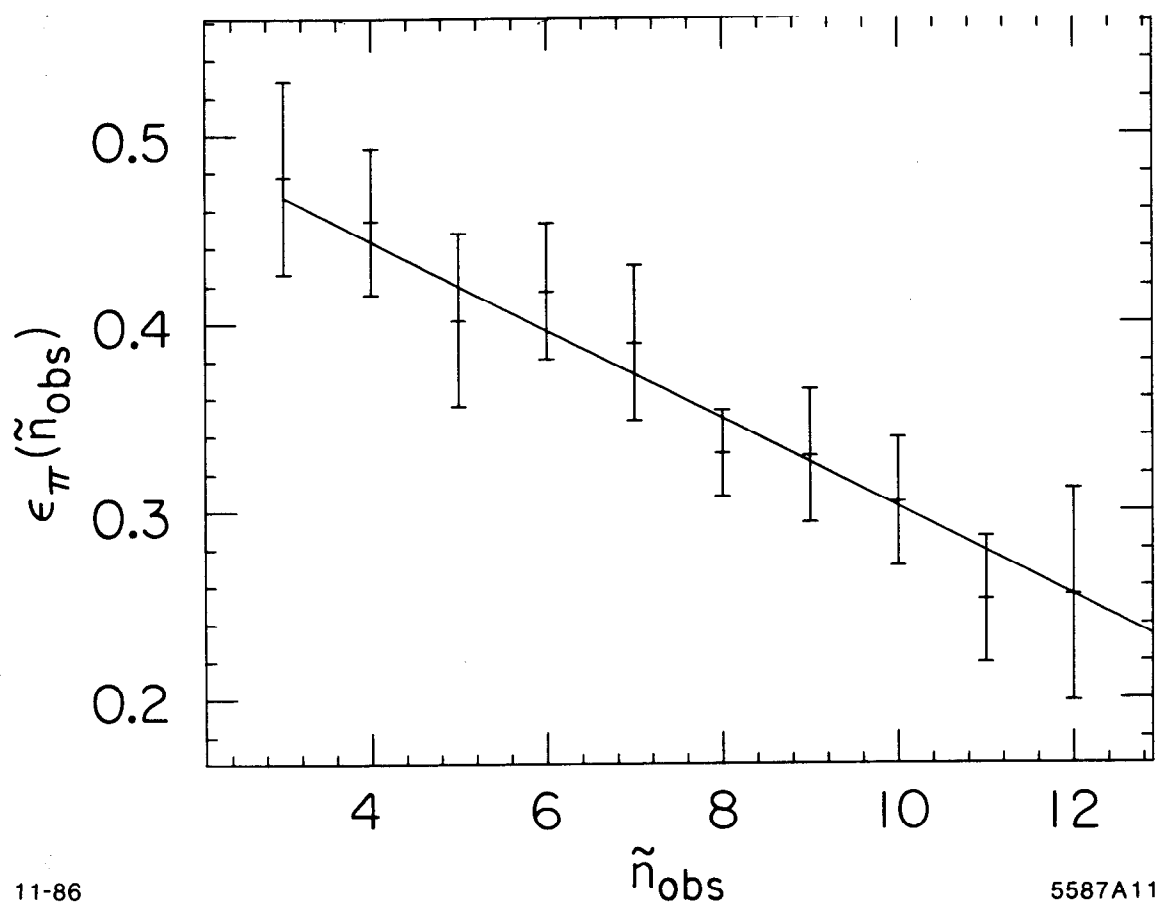


Fig. 11



11-86

5587A11

Fig. 12

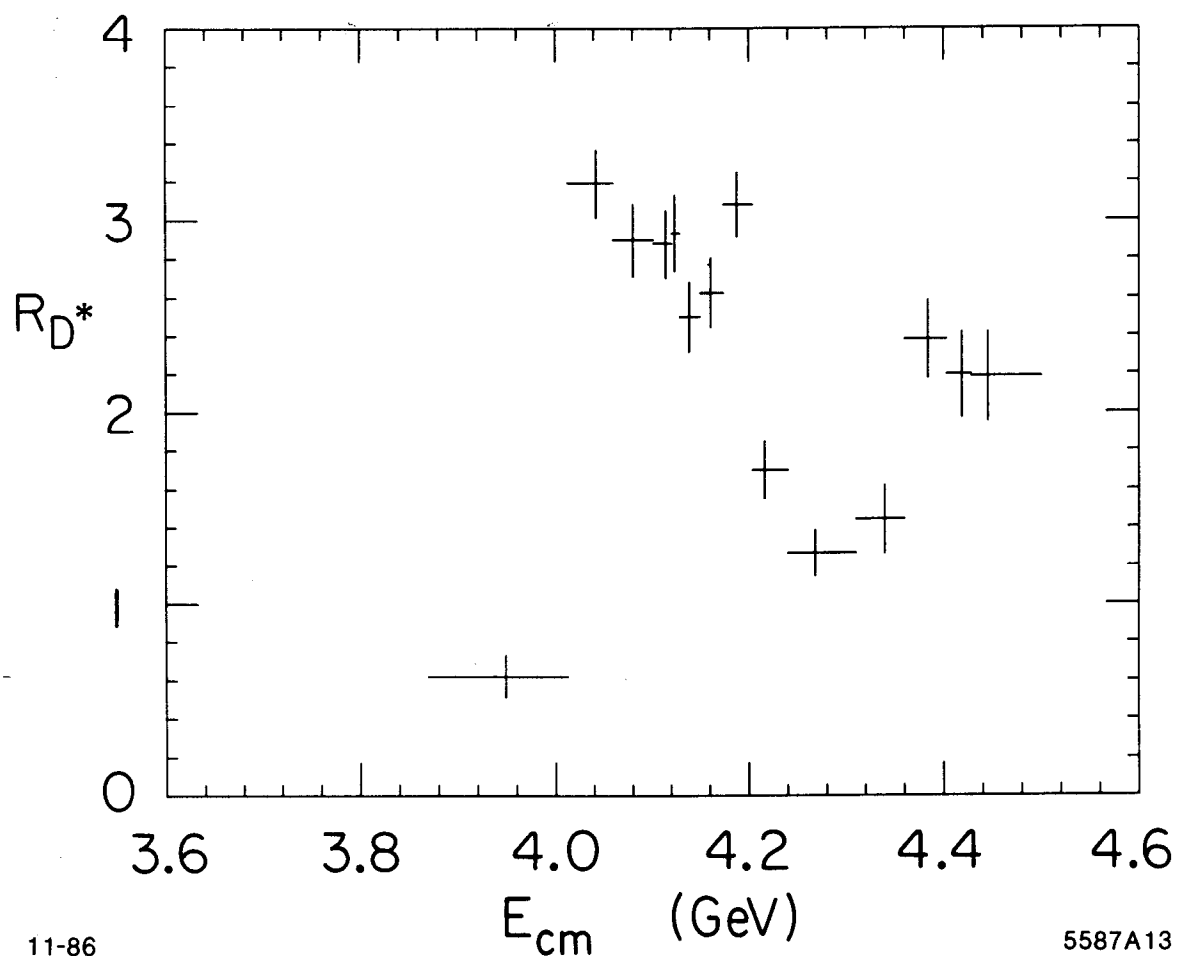


Fig. 13

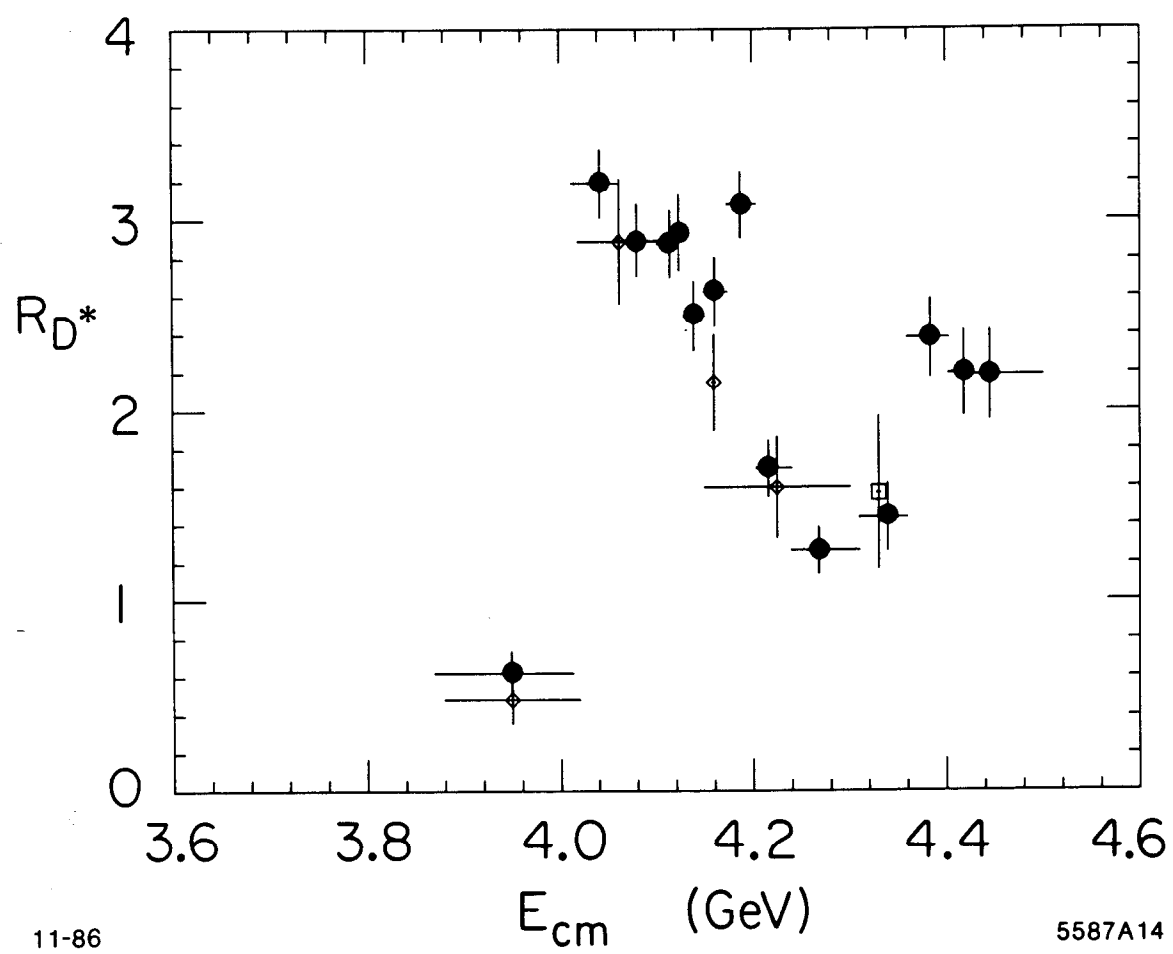


Fig. 14

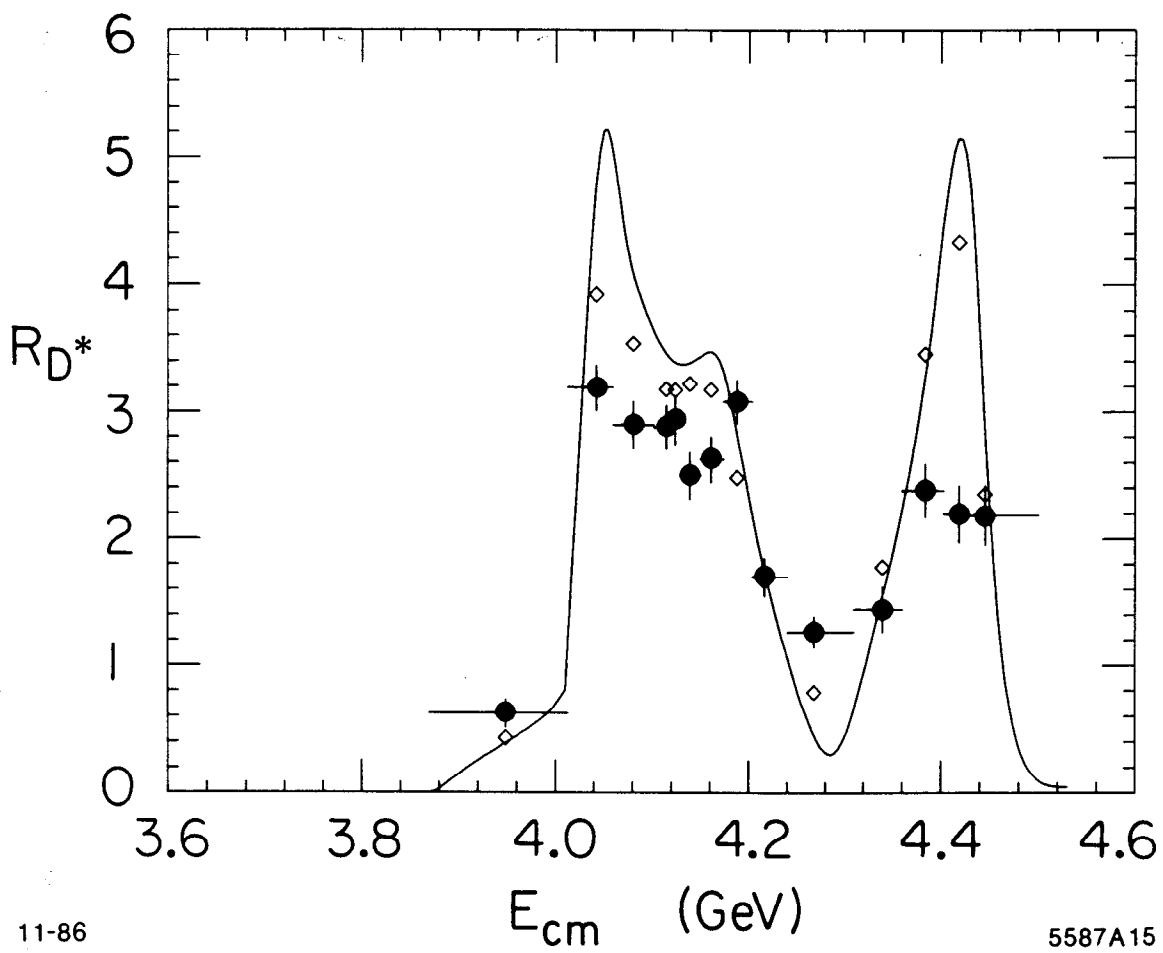
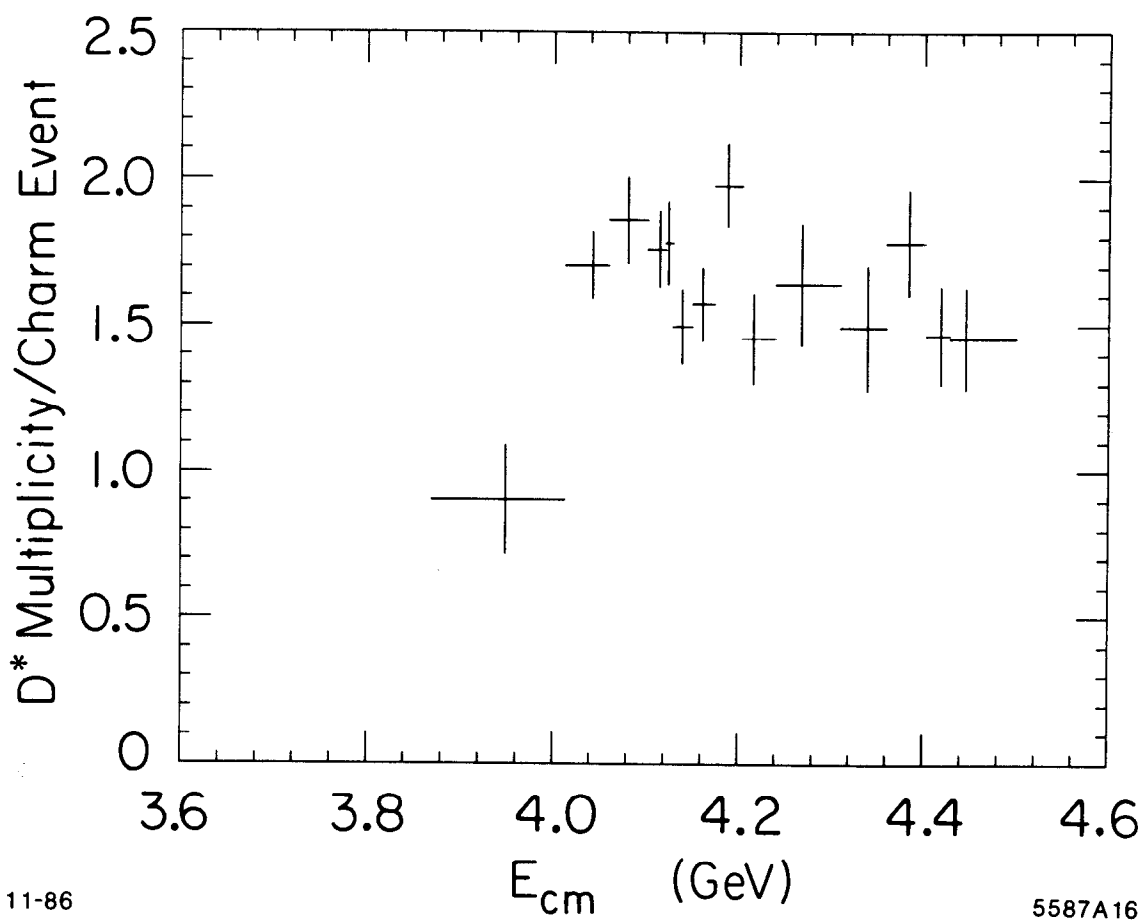


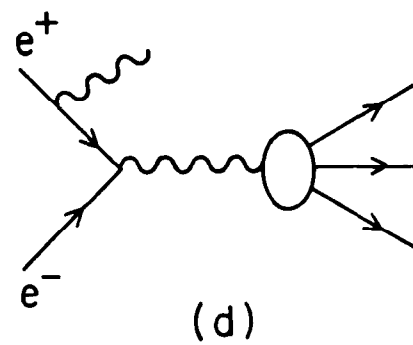
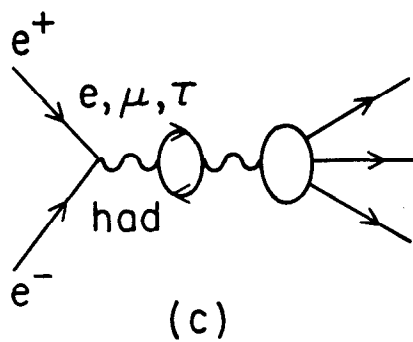
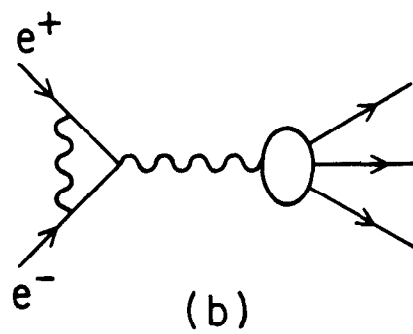
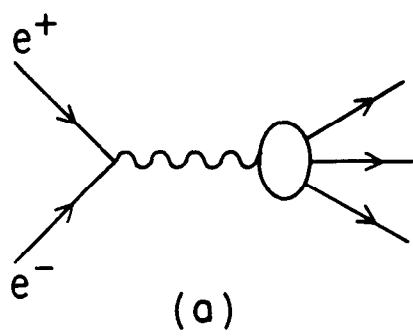
Fig. 15



11-86

5587A16

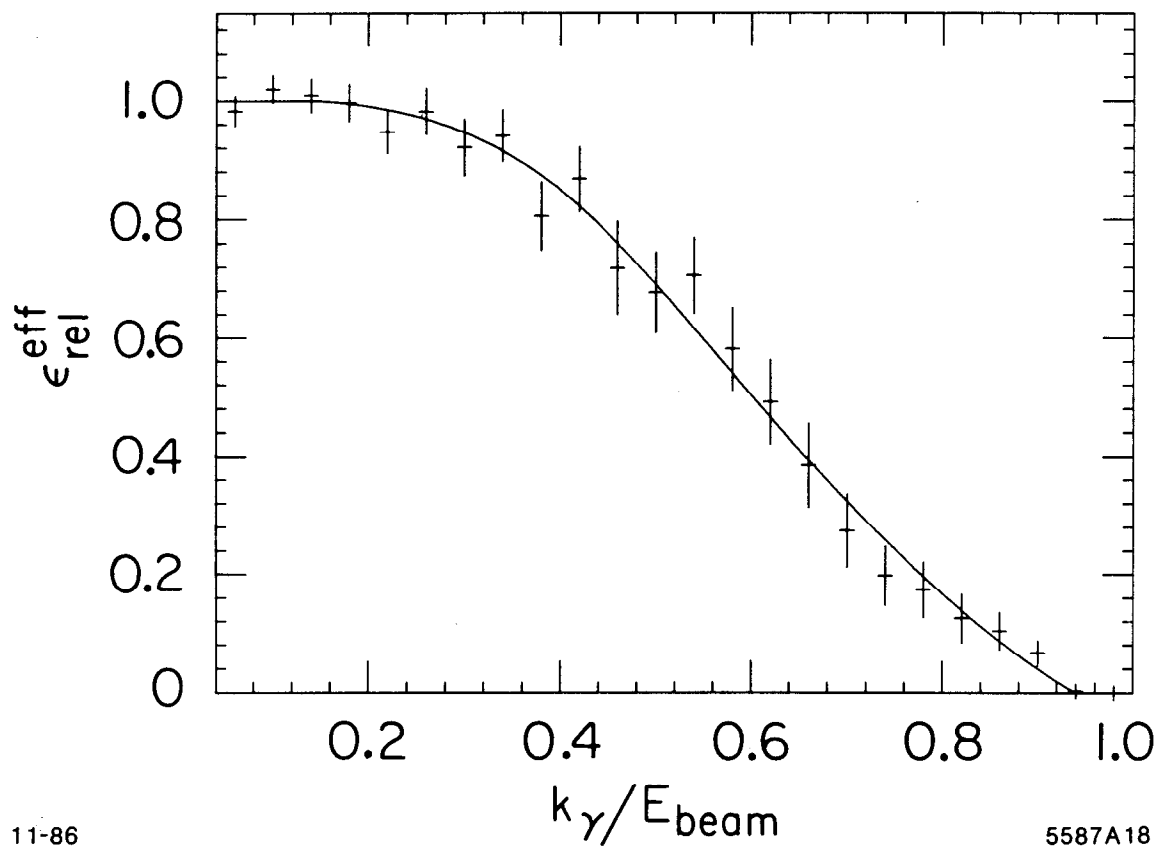
Fig. 16



11-86

5587A17

Fig. 17



11-86

5587A18

Fig. 18